Journal of Oceanology and Limnology
Vol. 42, No. 1, pp. 58-89, 2024
https://doi.org/10.1007/s00343-023-2347-7

Research Paper

Magmatic-tectonic response of the South China Craton to the Paleo-Pacific subduction during the Triassic: a new viewpoint based on Well NK-1*

Chan WANG[1, 2, 3, #], Hao LIU[4, #], Gang LI[1, 2], Zhen SUN[1, 2], Tingting GONG[3, 5], Li MIAO[1, 2], Xiaowei ZHU[1, 2], Yunying ZHANG[1, 2], Weihai XU[1, 2, **], Wen YAN[1, 2, 6, **]

[1] *Key Laboratory of Ocean and Marginal Sea Geology, South China Sea Institute of Oceanology, Chinese Academy of Sciences, Guangzhou 510301, China*

[2] *Southern Marine Science and Engineering Guangdong Laboratory (Guangzhou), Guangzhou 511458, China*

[3] *Key Laboratory of Tectonic Controlled Mineralization and Oil Reservoir of Ministry of Natural Resources, Chengdu University of Technology, Chengdu 610059, China*

[4] *School of Earth Sciences and Resources, China University of Geosciences (Beijing), Beijing 100083, China*

[5] *College of Earth Science, Chengdu University of Technology, Chengdu 610059, China*

[6] *University of Chinese Academy of Sciences, Beijing 100049, China*

Received Oct. 24, 2022; accepted in principle Nov. 29, 2022; accepted for publication Jan. 10, 2023

Abstract The Nansha Block (NB) is one of the blocks separated from the southern margin of the South China Craton (SCC) by the western Pacific subduction, which contains rich information of geodynamic and tectonic transformation. To reveal the essence of western Paleo-Pacific subduction during the Triassic period, Well NK-1 in this block was selected for petrographic study, and published research data from other cooperative teams were compared. A double-cycle pattern of basic to neutral magmatic volcanism was established, and 36 lithological rhythmic layers and representative cryptoexplosive breccia facies and welded tuff bands were identified. Combined with a reanalysis of published geochronological data, geochemical elements, and isotope geochemistry, we found that the rock assemblages could be divided into an intermediate-acid dacite (DA) series (SiO_2>65%) and basaltic (BA) series (Co<40 μg/g), which was formed during the early Late Triassic ((218.6±3.2)–(217.9±3.5) Ma). BA exhibits obvious calc-alkaline island-arc magmatic properties: $(^{87}Sr/^{86}Sr)_i$ ratio ranging 0.703 77–0.711 18 (average: 0.706 45), $^{147}Sm/^{144}Nd$ ratio ranging 0.119–0.193 (average: 0.168), and chondrite-normalized rare earth element (REE) curves being flat, while DA exhibits remarkable characteristics of subducted island-arc andesitic magma: $(^{87}Sr/^{86}Sr)_i$ ratio (0.709 39–0.711 29; average: 0.710 35), εNd(t) value (-6.2–-4.8; average: -5.6) and $\varepsilon_{Hf}(t)$ value (-2.9–-1.7, average: -2.2) show obvious crust-mantle mixing characteristics. BA and DA reveal typical characteristics of island-arc magma systems and type II enriched mantle (EM-II) magma. BA magma was likely resulted from the process whereby the continental crust frontal accretionary wedge was driven by the Paleo-Pacific slab subduction into the deep and began to melt, resulting in a large amount of melt (fluid) joined the asthenosphere on the side of the continental margin. In contrast, DA magma was likely resulted from the process whereby the plate front was forced to bend with increasing subduction distance, which triggered the upwelling of the asthenosphere near the continent and subsequently led to the partial melting of the lithospheric mantle and lower crust due to continuous underplating. The lithospheric thinning environment in the study area at the end of Triassic created suitable conditions for the separation between the NB and SCC, which provided an opportunity for the formation of the early intracontinental rift during the later expansion of the South China Sea (SCS).

* Supported by the National Natural Science Foundation of China (No. 42206073), the National Key R&D Program of China (No. 2021YFC3100600), the Guangdong Basic and Applied Basic Research Foundation (No. 2021A1515110782), the China Post-doctoral Science Foundation (No. 2021M703296), the Open Fund of the Key Laboratory of Tectonic Controlled Mineralization and Oil Reservoir of the Ministry of Natural Resources (No. gzck202101), the Key Special Project for Introduced Talents Team of Southern Marine Science and Engineering Guangdong Laboratory (Guangzhou) (No. GML2019ZD0206), and the K. C. Wong Education Foundation (No. GJTD-2018-13)

** Corresponding authors: whxu@scsio.ac.cn; wyan@scsio.ac.cn

# Chan WANG and Hao LIU contributed equally to this work and should be regarded as co-first authors.

Keyword: Paleo-Pacific tectonic domain; tectonic evolution; rift volcanic rock; Nansha Block; South China Craton

1 INTRODUCTION

The Pangea formed on a global scale with the merging of Gondwana between Laurasia during the Permian Period and was surrounded by an ocean known as the Panthalassa or the Paleo-Pacific (Gao et al., 2017; Yan et al., 2017; Hara et al., 2018; Xu et al., 2018; Luo et al., 2021). Later, the Paleo-Pacific gradually expanded and subducted along the eastern margin of Eurasia, resulting in large-scale intracontinental deformation and vast magmatic provinces (Xu et al., 2017; Liu et al., 2019a, b; Sun et al., 2020; Zhu et al., 2020); a cordillera-type linear mountain system extending thousands of kilometers formed on the western margin of the North and South American continents (Zhao et al., 2007, 2016; Li et al., 2018a). These two different subduction responses and their deep genetic mechanisms have aroused great interest from geologists (Zhang et al., 2021). The South China Craton (SCC), as a part of Eurasia, has experienced a series of important geological events (such as the Indosinian movement, Yanshanian movement, destruction of the SCC, and formation of large-scale metal mineral resources in the eastern SCC) under the influence of subduction of the Paleo-Pacific Plate and its superimposed effects (Hong et al., 2017; Li and Zhou, 2018; Hou et al., 2019; Sun et al., 2019; Liu et al., 2021a; Shu et al., 2021; Xie et al., 2021). The orogenic mode and dynamic mechanism of the southeastern margin of the SCC during the Permo-Triassic Indosinian movement have always been controversial. Some scholars think that the Hercynian-Indosinian movement was caused by the closure of the Jinshajiang-Ailaoshan-Song Ma branch ocean basin and the subsequent collision between the Indochina Plate and the SCC (Holloway, 1981; Hall, 2012; Ding et al., 2013; Jian et al., 2019; Chen et al., 2020). Other scholars assert that no collisional orogeny in South China occurred during the Permo-Triassic period but that a remote intraplate collisional orogeny was caused by the closure of the Paleo-Tethys Ocean between the Indochina Plate and the Sibumasu Plate (Jahn, 2010; Shao et al., 2015; Li et al., 2018b; Duan et al., 2020). Other scholars have proposed that tectonic movement was caused by the subduction of the Paleo-Pacific Plate along the southeastern margin of the SCC toward the northwest since the Permian (Wu and Suppe, 2018; Zhang et al., 2018).

The South China Sea (SCS) is a unique marginal sea located at the junction among the Eurasian Plate, Indo-Australian Plate, and Pacific Plate (Yi et al., 2021). Therefore, its formation and evolutionary history have always been a hotspot in the study of ocean-continental transition zones. The Nansha Block (NB), one of the many blocks in the SCS, was a product of the SCC detachment influenced by the Paleo-Pacific subduction mechanism (Luo et al., 2021). Geophysical data suggest that the NB has a Proterozoic folded continental basement that displays affinities with the SCC, which has been confirmed by Pb isotope data for the rocks (Zartman et al., 1988; Yan et al., 2011; Huang et al., 2013; Miao et al., 2021; Wei et al., 2022). Moreover, the NB separated from the Indochina-South China paleocontinent and drifted southeast and southward since the Late Cretaceous; these events are considered to have been caused by the far-field effect of the collision between the Indian Ocean Plate and the Eurasian Plate. Seafloor spreading was halted when the Australian Plate front subducted under the Sunda continent during the middle Miocene (Li et al., 2017; Li and Zhou, 2018). However, no direct petrological evidence has been reported for the above hypothesis, greatly hindering the in-depth study of the tectonic evolution of the NB. For example, when did the NB split from the SCC? What was the dissociation process? What role does the NB played in the formation and evolution of the SCS? Many issues require further exploration and analysis.

Triassic arc magmatic rocks, as important products of Paleo-Pacific subduction, play an important role in the reconstruction of the Paleo-Pacific subduction model on the southeastern margin of the SCC (Xie et al., 2021; Yang et al., 2021). In this study, we selected core samples from Well NK-1, which is a very important well drilled through volcanic rocks in the NB, southern SCS, as the research subject and extracted important geological information regarding the apparent nearly 1 100-m thick Triassic volcanic rocks. This paper presents a comprehensive study based on the detailed analysis of petrological, petrographic, and mineralogical characteristics of volcanic rocks in Well NK-1 and the sample test data obtained in previous work. The aims are to

establish a model of the magmatic eruption cycle, and characterized the magma source area, the genetic mechanism of volcanic rocks and the tectonic setting of magmatic dynamics, and finally to reveal the tectonic evolution process of the NB. This study promoted the understanding of the evolution of the Paleo-Pacific tectonic domain on the eastern margin of Eurasia, which effectively constrains the formation age of volcanic rocks in Well NK-1 and exploration of the affinity between the NB and SCC.

2 GEOLOGICAL SETTING

The SCS, one of the largest marginal seas in the western Pacific Ocean, is located at the junction of the three largest plates in the world at present: the Pacific Plate on the east, the Eurasian Plate on the north-northwest, and the Indo-Australian Plate on the south-southwest (Xu et al., 2012; Yi et al., 2021). The multiple extensional basins formed on the eastern margin of the SCS are closely related to the expansion of the SCS that began at ~34 Ma and stopped at ~16 Ma (Chen et al., 1992; Liu et al., 1997; Huang et al., 2013). Following the cessation of seafloor spreading, the intraplate oceanic island basalt associated with the Hainan mantle plume covered large areas of the SCS and its adjacent areas (e.g., Yan et al., 2011, 2017; Shao et al., 2015; Sun et al., 2020). The NB, located in the southwestern SCS, covers an area of approximately 60×10^4 km^2. Its northwestern boundary is a residual spreading ridge in the middle of the southwestern basin and a fault extending to the southwest. Its southern boundary is the Lupal fault. Its eastern boundary is the Zhongnan-Lile fault (Yan et al., 2011; Miao et al., 2021; Yi et al., 2021). There were four tectonic stages in the NB in the pre-Middle Mesozoic geology: (1) the Archean to the Paleoproterozoic (4 000–1 600 Ma) crystalline basement-formation, (2) the Mesoproterozoic to the Neoproterozoic (1 600–541 Ma) rifting, (3) the early Paleozoic (541–359 Ma) intracontinental orogeny, and (4) the early Mesozoic (251–200 Ma) Indosinian orogeny (Wang and Li, 2001, 2003; Zou et al., 2020, 2021; Liu et al., 2021b; Wang et al., 2021). Subsequently, the NB separated from the SCC and complex continental-ocean transition processes occurred from the middle of the Mesozoic to the Cenozoic Era.

3 PETROLOGY

This study is the first attempt to present high-resolution detailed observations and rock type divisions of the 975.3–2 020.2-m core column in Well NK-1, as well as the microscopic identification of 85 representative rock thin sections.

Optical thin section observations were conducted, and orthogonally polarized photomicrographs were obtained with a microscope (Carl Zeiss Axio Scope A1, Germany). All preparation of optical thin sections was completed at Guangzhou Tuoyan Testing Technology Co., Ltd., and laboratory identification was completed in the optical section identification room of the National Geology Experimental Teaching Demonstration Center of Chengdu University of Technology.

The bulk geochemistry, zircon U-Pb chronology, and Sr-Nd-Pd-Hf isotope data in this study were obtained from Miao et al. (2021) and Wei et al. (2022) (Supplementary Tables S1–S5).

3.1 Core sample characteristics

Well NK-1 is located on the Meiji Reef, an oval coral atoll in the central Nansha Islands 240 km away from southern Palawan Island (Fig.1). The total drilling depth was 2 020 m, and the core recovery percentage was 91%. A volcanic rock section with a thickness of 1 021.3 m was drilled (Fig.2), and its color changed clearly from dark to light from bottom to top (some of the core segments are interbedded) at macro level. The volcanic rock segment underlies gray-black quartz sandstone and overlies gray-white mixed deposits of clastic/carbonate/reef sediments. According to the division model of volcanic eruption cycles and subcycles, the first cycle of mafic→neutral magmatic volcanism is evident from 2 017.5 m to 1 290.2 m, and the second cycle of mafic→intermediate-felsic magmatic volcanism appears from 1 290.2 m to 996.2 m. The first cycle can be further divided into a mafic magma eruption subcycle (2 017.5–1 963.2 m)→mafic magma overflow subcycle (1 963.2–1 469.2 m)→neutral magma overflow subcycle (1 469.2–1 290.6 m). The second cycle is further divided into a mafic magma overflow subcycle (1 290.6–1 131.5 m)→neutral-mafic magma overflow subcycle (1 131.5–1 077.8 m)→intermediate-felsic magma overflow subcycle (1 077.8–996.2 m). Pelitic tuff at 1 263.7–1 267.4 m, lenticular welded tuff bands at 1 275.2 m, and tabular volcanic gravel at the top of volcanic rocks in the second cycle are also present, suggesting that the magma was a distinct underwater eruption (Wu et al., 2019). This combination of multiple rhythms and numerous cycles is the comprehensive result of multiple magma eruptions and evolution (Gong et al., 2021b).

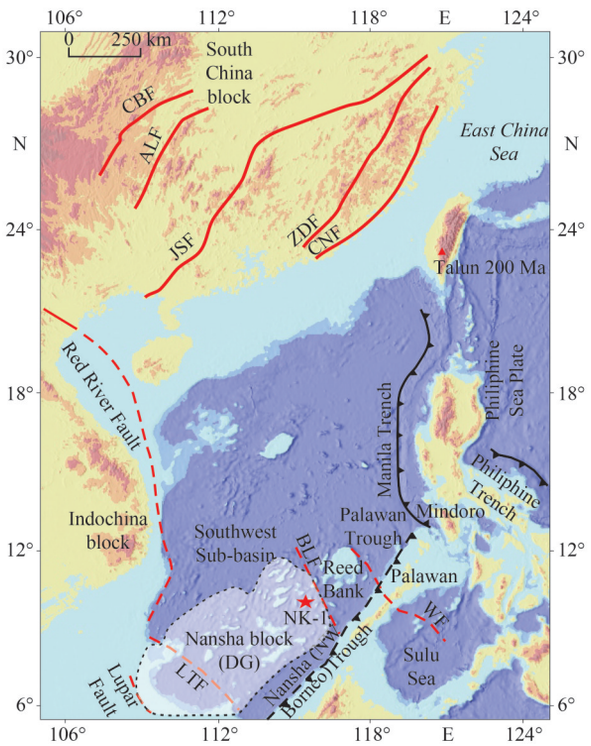

Fig.1 Survey of the research area and drilling location (after Miao et al., 2021)

CBF: Cili-Baojing Fault; ALF: Anhua-Luocheng Fault; JSF: Jiangshan-Shaoxing Fault; ZDF: Zhenghe-Dapu Fault; CNF: Changle-Nanao Fault; WF: Wulugen Fault; BLF: Balabac Fault; LTF: Lizhun-Tinjia Fault. Red star means the location of samples from Well NK-1.

3.2 Microscopic characteristics

The petrographic characteristics are newly reported in this paper. Based on the core catalog and detailed identification of 53 rock slices, the first and second cycle characteristics of lithologic facies are clear, at the boundary of approximately 1 400 m; the first cycle consists of basaltic andesite and a combination of trachyte-trachyandesite (Fig.2). The second cycle contains mainly a set of alterations of pyroxene-bearing basalt, basaltic trachyandesite-trachybasalt, and trachyandesite-trachydacite with local tuff lava assemblages. The lavas all have porphyritic structures, and welded tuff or tuff lava textures can be seen in tuff lavas.

The phenocrysts are mainly composed of feldspar and dark minerals, with a small amount of quartz in the second cycle.

Andesine: This mineral is found in all types of lavas and tuff lavas; grains are mostly idiomorphic-hypidiomorphic and tabular and often develop alteration and twin crystals. In the late stage, weak to moderate saussuritization, epidotization, potassic alteration, and clayization occurred. The direction of plagioclase twin-crystal binding in the upper cycle is inclined in the (010) direction; in addition, alkaline feldspar coronas can be seen at the margins (Fig.3a), or grains are embedded with each other and have a distributed glomeroporphyritic texture (Fig.3b). Moreover, some grains in trachyte and trachybasalt display twin-crystal deformation and sand bell-type structures.

Dark minerals: These minerals are common in trachybasalt and trachyandesite in the two cycles, which have no complete and fresh grains; however, the shapes of early euhedral columns (similar to amphibole or alkaline pyroxene, such as aegirine-augite and aegirine) are retained, and the particle sizes are within 1 mm. Many inclusions, such as apatite, are common, and some particles occasionally retain dark edges. The alteration characteristics show that the stages are in the order of high-temperature actinolitization→lepidolitization (chlorite of the high-temperature phase)+epidotization+ silicification and lower-temperature chlorite and carbonation.

Alkali feldspar: These grains are distributed in trachyandesite and trachyte and are mainly perthite; orthoclase retains the sanidine in shape. The perthite has developed a variety of perthitic textures and types; for example, evidence of sanidine can be seen in Carlsbad twins and cleavage in the direction of oblique crossing (001) (Fig.3c). Inlaid metasomatic plagioclase can be observed in the first cycle, although metasomatism is weak overall, and zoisitization is relatively strong. In the second cycle, a few alkaline feldspars are independent minerals, while the remainder are metasomatic plagioclases with “trim shapes” and “patch shapes”, and the main alteration is kaolinization.

Quartz: This mineral is rounded and occasionally found in the upper trachydacite, where it retains an atypical high-temperature β-quartz morphology (Fig.3d).

Matrix: A palimpsest vitreous texture (retained arc compression textures) (Fig.3e) can be seen in the trachyandesite, trachyte, and trachydacite matrices, with conversion to trachyte-cryptocrystalline texture after recrystallization, but spherules that are not completely devitrified are commonly retained. The composition consists of feldspar, a few dark minerals, and cryptocrystalline and dusty iron aggregates. The relatively coarse matrix in the basalt-basaltic andesite is composed of feldspar microcrystals (mostly sericite+clayization+epidotization) (Fig.3f) and

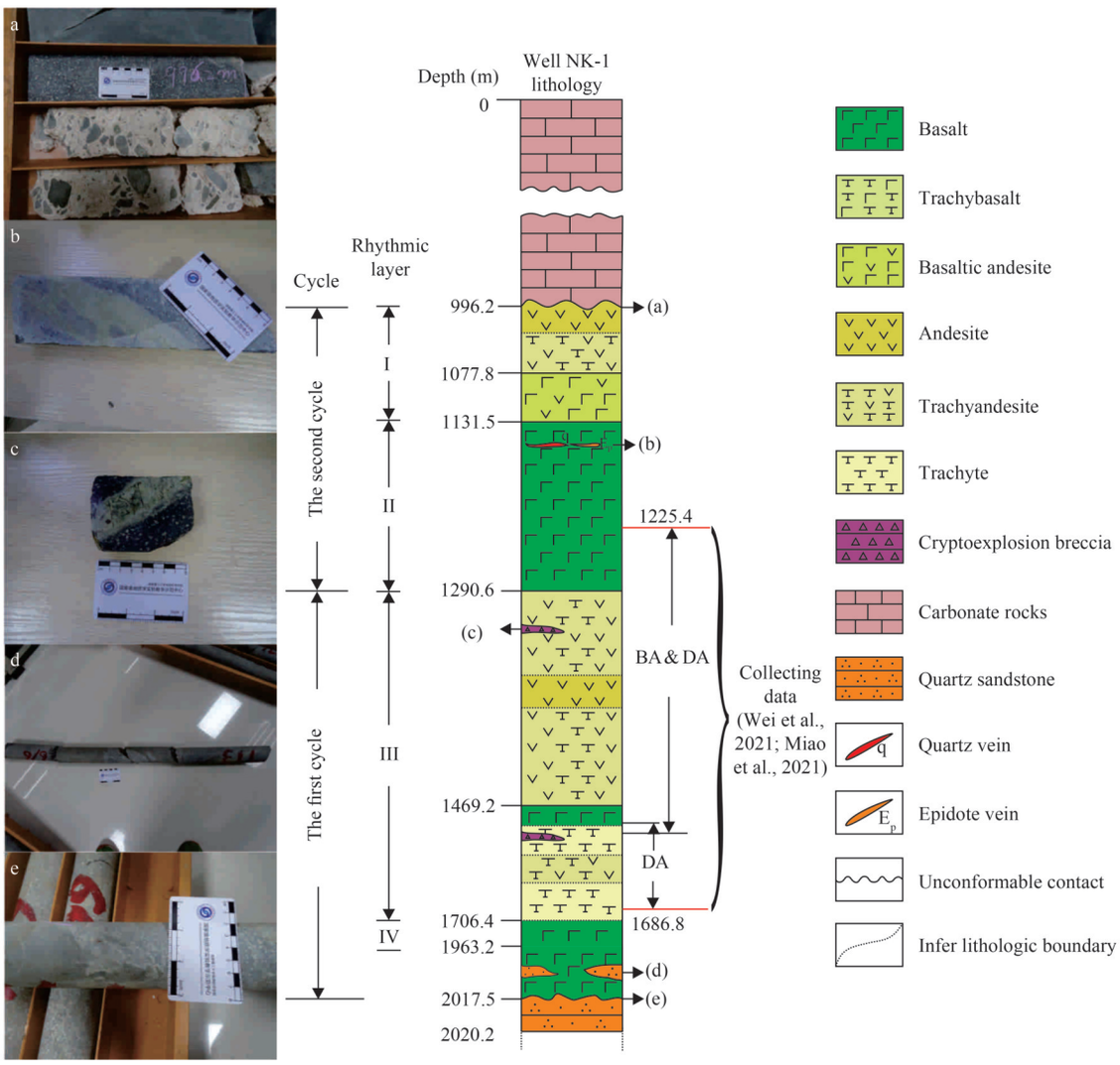

Fig.2 Lithological column sketch diagram of volcanic rock in Well NK-1

a. unconformity between carbonate rock and volcanic rock at 996.2 m; b. an epidote vein and a quartz vein at 1 139 m; c. cryptoexplosive breccia seen in the core; d. basalt blocks embedded in quartz sandstone with angular or fused rounded edges, implying that the quartz sandstone was caused by magma blasting after corrosion solidification; e. unconformity between volcanic rock and carbonate rock at 2 017.5 m. I: the andesite rhythmic layer, microcrystalline-cryptocrystalline trachyteandesite and porphyritic dacite rhythmic layer, and microcrystalline-cryptocrystalline basaltic andesite and porphyritic-containing basaltic andesite rhythmic layer (a total of 3 layers); II: the (porphyritic-containing) porphyritic basalt and microcrystalline-cryptocrystalline basalt layers (a total of 7 layers); III: the microcrystalline-cryptocrystalline trachyteandesite and porphyritic trachyteandesite layers (a total of 10 layers); IV: the cryptocrystalline basalt and porphyritic basalt layers (a total of 16 layers).

dark minerals (pyroxene/amphibole in the early stage plus actinolite, biotite, chlorite, muscovite, etc.) with a mostly intergranular-intersertal texture and local pilotaxitic texture.

In addition, amygdaloid bodies filled with quartz+epidote and occasionally with calcite are sporadically found in the lower BA.

In some tuffaceous-bearing lavas, a few plastic magma fragments, crystals, and rigid homologous detritus can be found, and tension-shear fractures have developed in the rocks, which are filled with lepidolite+ rectangular/deformed quartz, contemporaneous with the alteration of dark minerals.

Among the accessory minerals, the volcanic rocks from Well NK-1 in the SCS generally form a titanomagnetite-apatite-zircon assemblage rich in zircon, apatite, and other minerals with incompatible elements.

Apatite: This mineral is distributed mainly in the two cycles in the form of long columns, acicular columns, hexagonal columns, and hexagonal bipyramids. Some apatite grains contain fine apatite grains or other minerals, particles of metallic minerals and gas and liquid inclusions.

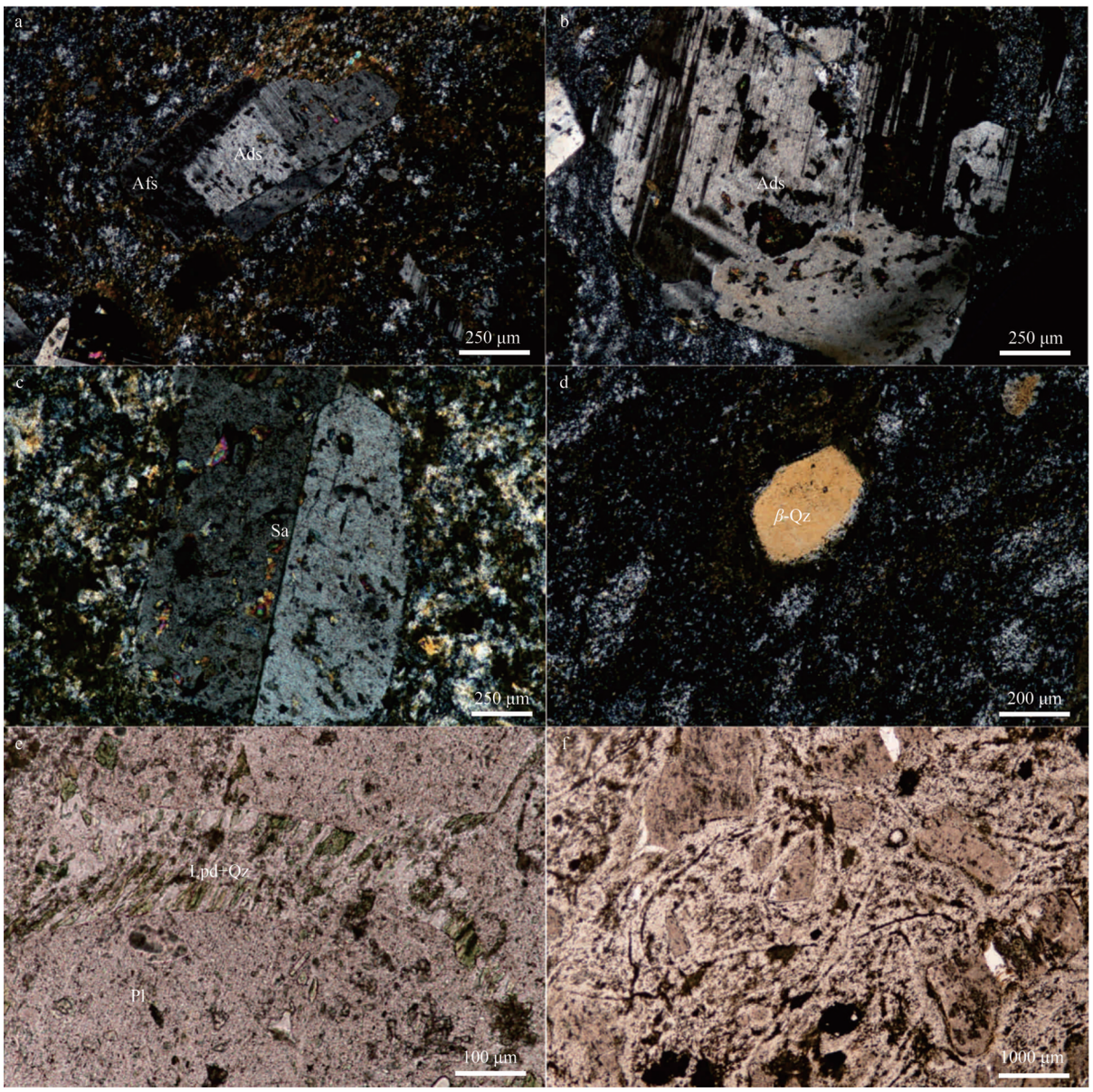

Fig.3 Microscopic characteristics of Well NK-1 volcanic rocks

a. andesine phenocryst with an alkaline feldspar border (+); b. andesine glomerocryst with local mosaic growth (+); c. Carlsbad twins are developed in the sanidine phenocryst, and the alteration minerals on the right monomer are distributed parallel to each other crossing obliquely in the (001) direction (+); d. quartz phenocryst retains high-temperature β-quartz (β-Qz) morphology (+); e. tensional and shear fractures are developed in plagioclase phenocryst filled with rectangular lepidolite+quartz (-); f. the matrix has a vitreous texture and retains the typical arc-shaped contraction pattern (-). Ads: andesine; Afs: alkali feldspar; Lpd: lepidolite; Pl: plagioclase; Qz: quartz; Sa: sanidine.

Titanomagnetite: This mineral is mostly distributed in the lower part, with contents of 0.5–2 vol.% and relatively few fresh particles; the grains are mostly decomposed and partially or completely converted to an aggregation of leucosphenite+sphene, with three groups of residual cleavage remaining.

Zircon: Trace zircon grains were found in the two cycles; they display positive high relief and tertiary interference colors and have magmatic zircon shapes. A small fraction of the grain face is incomplete and may have burst.

Late tensile-shear fractures have developed in the rocks, and most of these fractures are filled with deformed rectangular quartz+lepidolite.

According to the mineral characteristics of the rocks, titanomagnetite and zircon crystallized earlier among the accessory minerals, while apatite may have had a longer crystallization time span.

In summary, the lithographic characteristics show that the rocks in the early magmatic cycle (in the

first cycles) crystallized with a large amount of volatile apatite and that the phenocryst mineral assemblage is dominated by plagioclase+pyroxene/hornblende. The magma was calc-alkaline to moderately alkaline and relatively mafic with high volatility. However, the content of K-feldspar among the phenocrysts of the second magmatic cycle obviously increases, clearly indicating that the magma source region underwent a transformation (Wang et al., 2018).

4 DISCUSSION

4.1 Classification of rock types

Based on the first detailed core characteristics analysis of Well NK-1, combined with the geochemical data published by other teams (Miao et al., 2021; Wei et al., 2022), the development of volcanic eruptions producing rhythmic layers and cycle assemblages indicate the continuation of magmatic eruption (Valentine et al., 2014). However, the alternate lithology evolution during this process suggests that the tectonic environment may be complex (Li, 1993). The microscopic characteristics show obvious two-cycle differences, and the characteristics of the first cycle imply that the mineral assemblage of the early phenocrysts was plagioclase+pyroxene+hornblende, with apatite that crystallized early. In general, the characteristics are reflected by calc-alkaline and mafic rocks, while the magma is rich in volatile components. A small number of plagioclase grains underwent orthoclasation/sanidinization in the later period, with polysynthetic twins crossing obliquely in the (010) direction; these features may indicate that the magma changed in the direction of slightly alkaline composition, potassization, and rapid dehydration, which are characteristic of multisource magma or fluid containing molten lava (Le et al., 1986). The observation of the grains in the second cycle shows autogenous sanidine and quartz phenocrysts, and the potassization is obviously weaker than that in the first cycle, which reflects the evolutionary trend of a homogeneous magma enriched in Si and K. Geochemical data were collected from 79 samples within the 1 489–1 225.4-m rhythmic interval spanning the first and second cycles and 1 485–1 686.8-m rhythmic interval covering the first cycle (Supplementary Tables S1–S3). The sample data in the study area fall into the basic basalt and intermediate-acid trachyte/trachyte dacite areas in Fig.4a, and combined with the characteristics of calc-alkaline basalt and high-K and shoshonite series dacite areas in Fig.4b, the volcanic rock cores of Well NK-1 are divided into the intermediate-acid DA and the basic BA in this paper.

4.2 Magma evolution process

4.2.1 BA evolution process

BA from Well NK-1 showed less variable SiO_2 content (47.09–53.37 wt.%, average 49.94 wt.%) and fluctuating MgO content (4.53–11.47 wt.%, average 6.91 wt.%). The negative correlation between MgO and SiO_2 and Al_2O_3, positive correlation between CaO/Al_2O_3, Ni and Cr, and positive correlation between TFe_2O_3, TiO_2, and P_2O_5 (Fig.5) show that magma in the BA source area had weak fractional crystallization of olivine, pyroxene, titanic oxide, and apatite, which is consistent with the titanomagnetite and apatite observed in the maceral

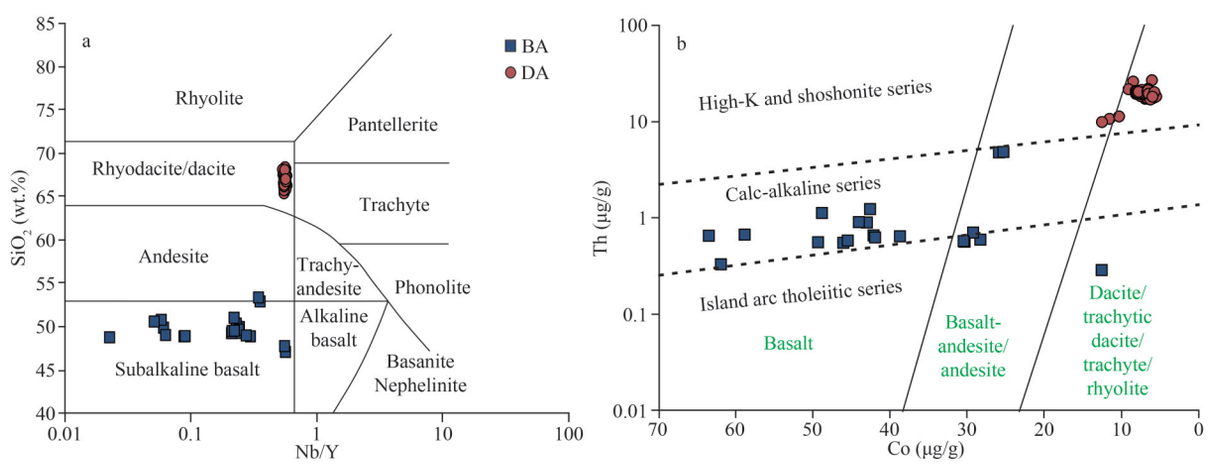

Fig.4 SiO_2 (wt.%) vs. Nb/Y diagram (after Winchester and Floyd (1977)) (a) and Th (μg/g) vs. Co (μg/g) diagram (after Stevenson (2018)) (b)

analysis in Section 3.2. The relatively continuous data distribution also indicates that the BA could be originated from a unified parent magma chamber (Liu et al., 2019c). The low TiO_2 contents (0.60 wt.%–2.10 wt.%; average: 1.15) and light rare earth element (LREE)/heavy rare earth element (HREE) >1 (0.70–2.84; average: 1.20) of the BA also suggest that the magma in the source region may have undergone a low degree of crystallization differentiation (Pearce and Norry, 1979).

The linear relationship of the BA data is in overall consistent with the trend of partial melting (Fig.6), which indicates that the magma chamber was dominated by partial melting with a degree of fractional crystallization (Patiño Douce and Beard, 1995). This is consistent with the CIPW calculation results for the BA (the differentiation index (DI) value ranges from 21.66 to 52.88, with an average value of 33.90, and the solidification index (SI) value approaches that of the initial magma, i.e., 23.44–45.99, with an average of 31.44). These characteristics also confirm that BA geochemical

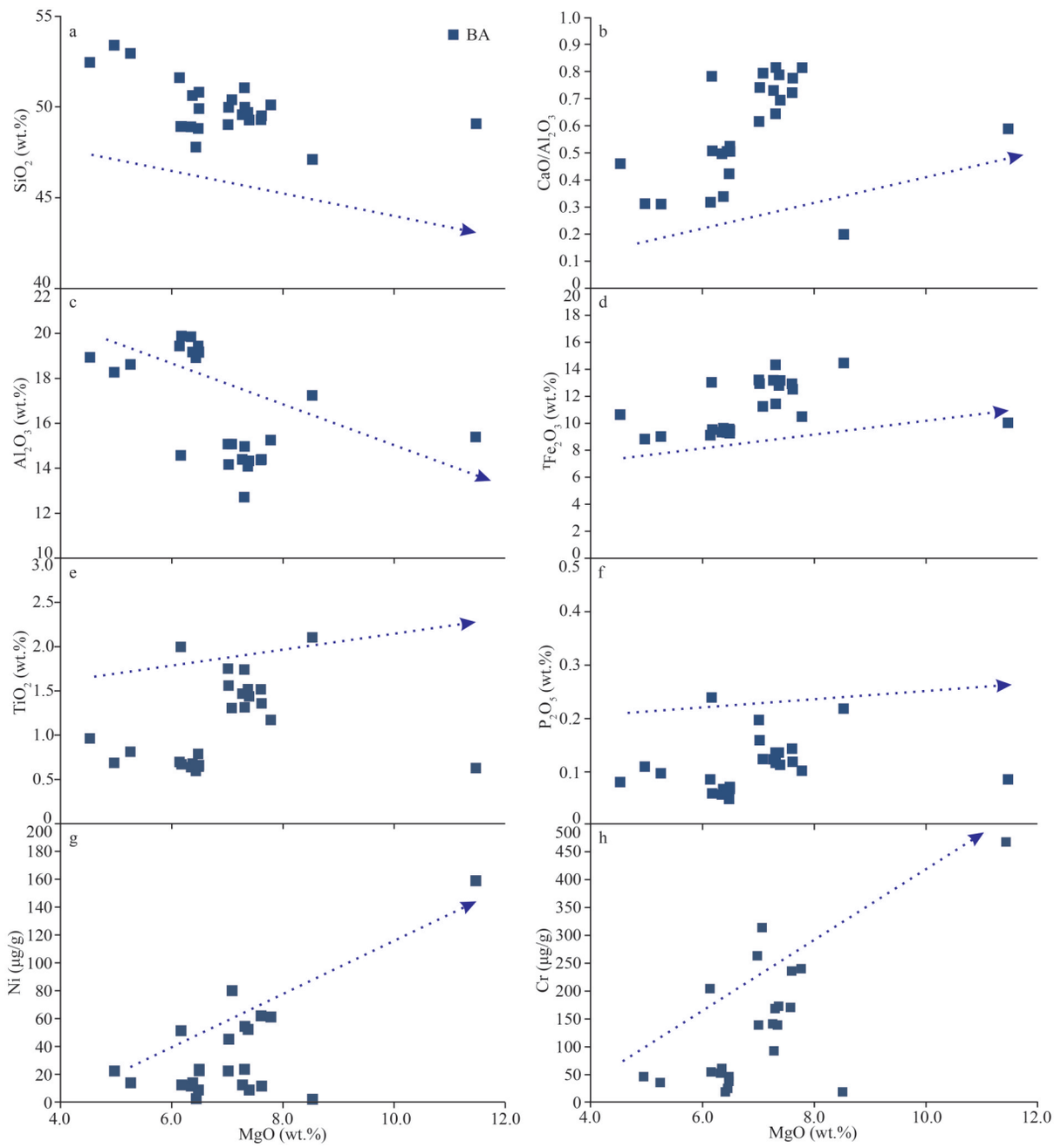

Fig.5 Bivariate plots of selected characteristic components vs. MgO (wt.%) of BA from Well NK-1

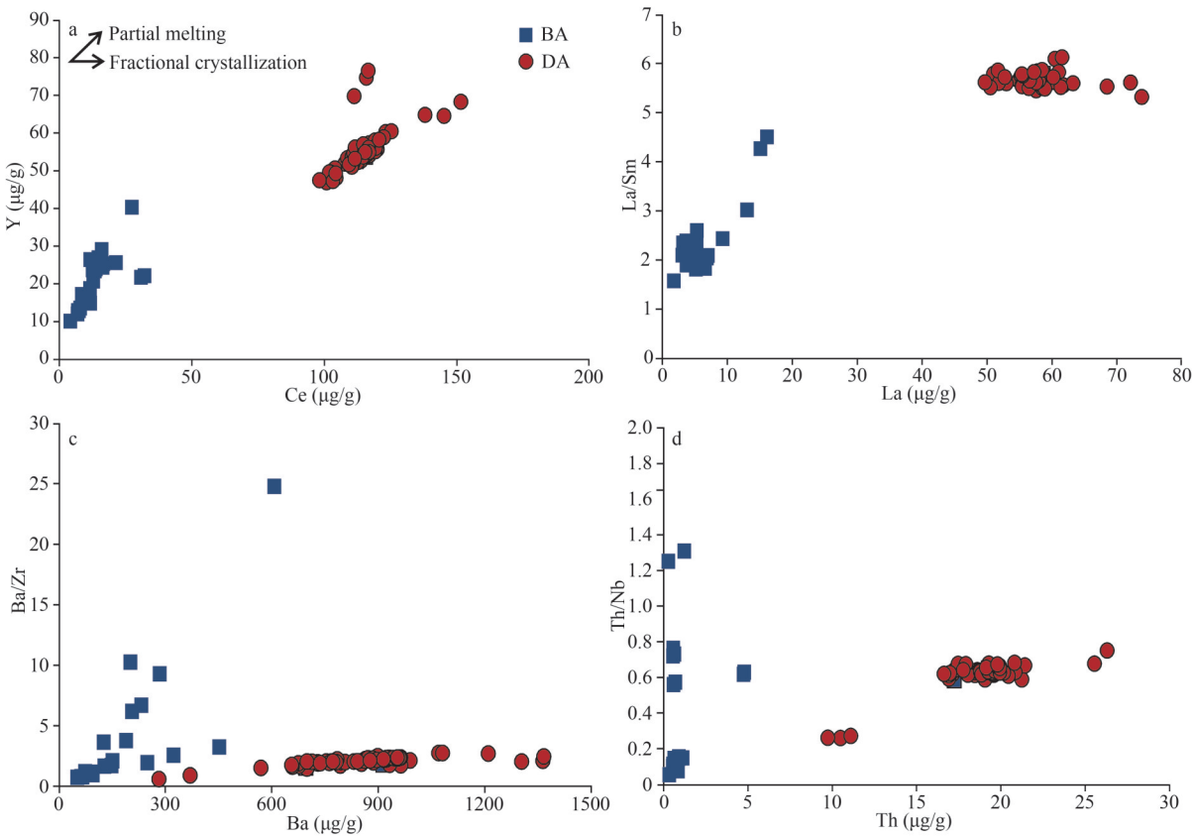

Fig.6 Binary diagrams illustrating the Y (μg/g)-Ce (μg/g) (a), La/Sm-La (μg/g) (b), Ba/Zr-Ba (μg/g) (c), and Th/Nb-Th (μg/g) (d) compositions of BA and DA rocks from Well NK-1

data have good indicative significance for the recovery of magma source areas (Rapp and Watson, 1995). BA data largely fall into the stable melting zone of spinel at <80-km depth (Fig.7a), which shows that the magma chamber in the source area was located in the transition region between the upper mantle asthenosphere and subcontinental lithospheric mantle (SCLM). In the partial melting trend diagram (Fig.7a), BA samples plot between the enriched mid-ocean ridge basalt (E-MORB) and primitive mantle (PM) fields, showing an enrichment trend, which is highly consistent with

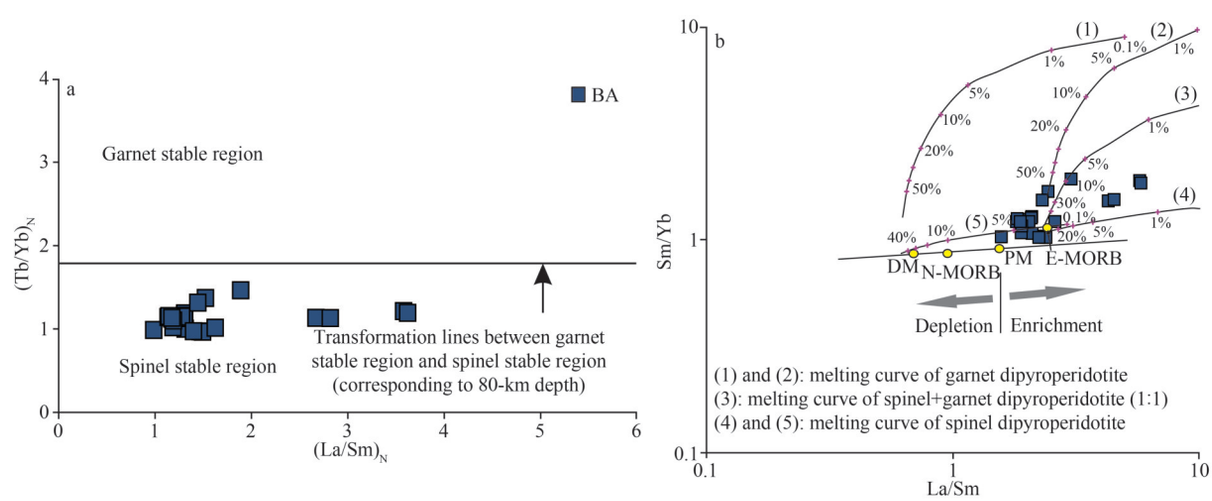

Fig.7 $(Tb/Yb)_N$ vs. $(La/Sm)_N$ diagram (a) (after Wang et al. (2019)) and Sm/Yb vs. La/Sm diagram (b) (after Li et al. (2018a))

DM: depleted mantle; PM: primitive mantle; N-MORB: normal mid-ocean ridge basalt: E-MORB: enriched mid-ocean ridge basalt.

curve (5) in Fig.7b. However, the data points near curve (3) in Fig.7b indicate that the magmatic source region may have also experienced partial melting of spinel+garnet lherzolite (the partial melting degree is 10%–20%). Because the contents of Zr (average: 111.13 μg/g) and Hf (average: 2.67 μg/g) in BA are lower than those in the (upper continental crust) UCC (the average values are 190 μg/g and 5.8 μg/g, respectively) (Supplementary Table S2), it is concluded that the magma in the source area was not obviously affected by crustal contamination during the ascent process (Gao et al., 2017).

4.2.2 DA evolution process

Compared to those of the UCC, DA exhibited a higher LREE/HREE ratio (average: 2.81), greater enrichment of large-ion lithophile elements (LILEs, such as Rb and K) and high-field strength elements (HFSEs) (such as Th, U, Zr, and Hf) and greater depletion of LILEs (such as Sr) (Fig.8). Combined with the higher DI value (average: 79.2) and lower SI value (average: 6.6) calculated by DA CIPW, the andesitic magma chamber in the study area experienced obvious crystallization differentiation (Gardien et al., 1995), which is consistent with the characteristics of the dominant fractional crystallization in the magma chamber of the DA source area, as shown in Fig.6. In the fractional crystallization and assimilation discrimination diagram (Fig.9), DA is dominated by fractional crystallization, but the degree of fractional crystallization is weak (Fig.9d), which indicates that the obvious element geochemical fractionation characteristics of DA should reflect fractional crystallization in the source region. The geochemical characteristics of DA are significantly different from those of BA, and the trace elements and REEs are significantly different, which suggests that the two types of rocks may derive from different magma sources (Iwamori and Nakamura, 2015).

DA samples show good continuity in Harker diagram (Fig.10), which should be the product of magma evolution in the same source area (Wang et al., 2019). The contents of MgO, CaO, Al_2O_3, TFe_2O_3, TiO_2, P_2O_5, Sr, and Cr in the DA samples decreased significantly with the increase in SiO_2 content, at the same time, combined with the obvious depletion of Ba, Eu, Nb, Ta, and Ti in DA. These results indicate that the magma in the DA source area experienced fractional crystallization of mafic minerals (such as pyroxene and amphibole), oxides containing Fe-Ti (such as titanomagnetite), plagioclase, K-feldspar, and apatite (Le and Thompson, 1988). In the Sr-Rb vs. Ba-Sr diagram (Fig.11), DA shows characteristics consistent with the trend line of biotite (Bi), suggesting that the source region may be water-rich and mafic-rich, which is also consistent with the enrichment of biotite minerals reflected in macerals in Section 3.2.

The origin of the parent magma of DA is worth discussing. Based on the discrimination diagram of multiple source areas, most DA samples fall into the overlap area of the partial melting of metasandstone and partial melting of the basic rock field (Fig.12a) and of the A-type granite formed by partial melting of intermediate-basic igneous rocks and biotite gneissic rock-derived melt field (Fig.12b–d). This feature suggests that the magma in the DA source area of the study area has obvious subduction arc properties, which is most likely due to partial

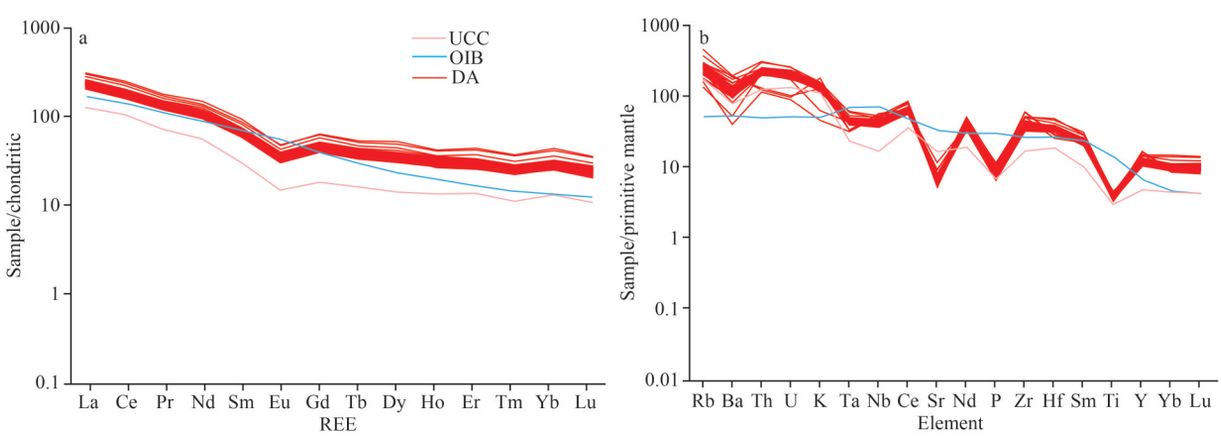

Fig.8 Chondrite-normalized REE distribution pattern of the DA (a); primitive mantle-normalized spider diagram of DA (b), normalized after Sun and McDonough (1989)

UCC (upper continental crust) and oceanic island basalt (OIB) data are from Taylor and McLennan (1985).

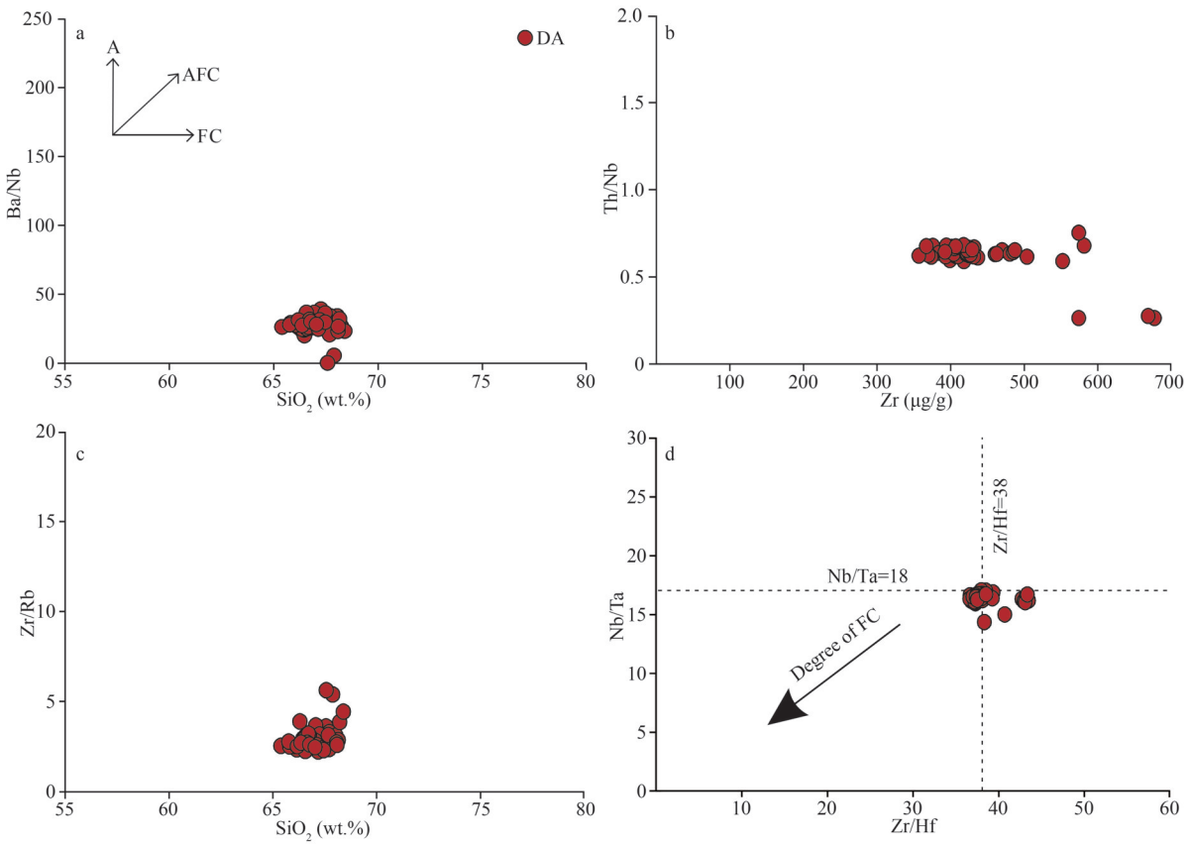

Fig.9 The fractional crystallization (FC) and assimilation (A) on the evolution of the magma producing the subvolcanic rocks (after Nicolae and Saccani (2003))

melting of continental lithospheric mantle and lower crust (Defant and Drummond, 1990; Li et al., 2018a). Figure 12e–f shows that the DA samples fall nearby sandstone source rock and shale, showing high agreement with sand-rich protolith and clay-poor source regions, which is similar to the characteristics of the Bethanga pluton in the Lachlan Fold belt, Australia. These characteristics suggest that the DA source area has obvious crust-mantle mixing characteristics rather than the partial melting of a single crust-derived material (Stevenson, 2018). Moreover, the geochemical element enrichment characteristics of DA are more obvious than those of UCC.

The basic and intermediate-acidic rock assemblages in Well NK-1 show geochemical characteristics similar to those of island-arc magmas. BA obviously belongs to the island-arc calc-alkaline basalt, while DA shows the characteristics of island-arc andesitic magmas, which originated from different magma chambers (Xu et al., 2017; Wei et al., 2022). The magma in the BA source area is dominated by the partial melting of spinel and garnet lherzolite with weak fractional crystallization (fractional crystallization of mafic minerals, minerals containing Fe-Ti and apatite). Geochemistry shows the trend of the chondrite-normalized REE curve similar to that of PM (Fig.13a) and the PM-normalized curve similar to that of (lower continental crust) LCC (Fig.13b). The geochemical characteristics of DA show that the source area is influenced by crust-mantle interactions, and the magma evolution shows limited crystallization differentiation and weak assimilation and contamination. Fractional crystallization is mainly dominated by the biotite phase with the addition of the fractional crystallization of mafic minerals, minerals containing Fe-Ti, apatite, plagioclase, and K-feldspar. The rock properties of BA and DA suggest that they originated during the mature island-arc stage influenced by the subduction of the western Pacific Ocean and were constrained by complex magmatism under the influence of subduction-related tectonics (Gao et al., 2017; Hernández-Uribe et al., 2020). The interbedded production of BA and DA rocks revealed by petrographic characteristics indicates that the late magma chamber eruption mode was dominated by

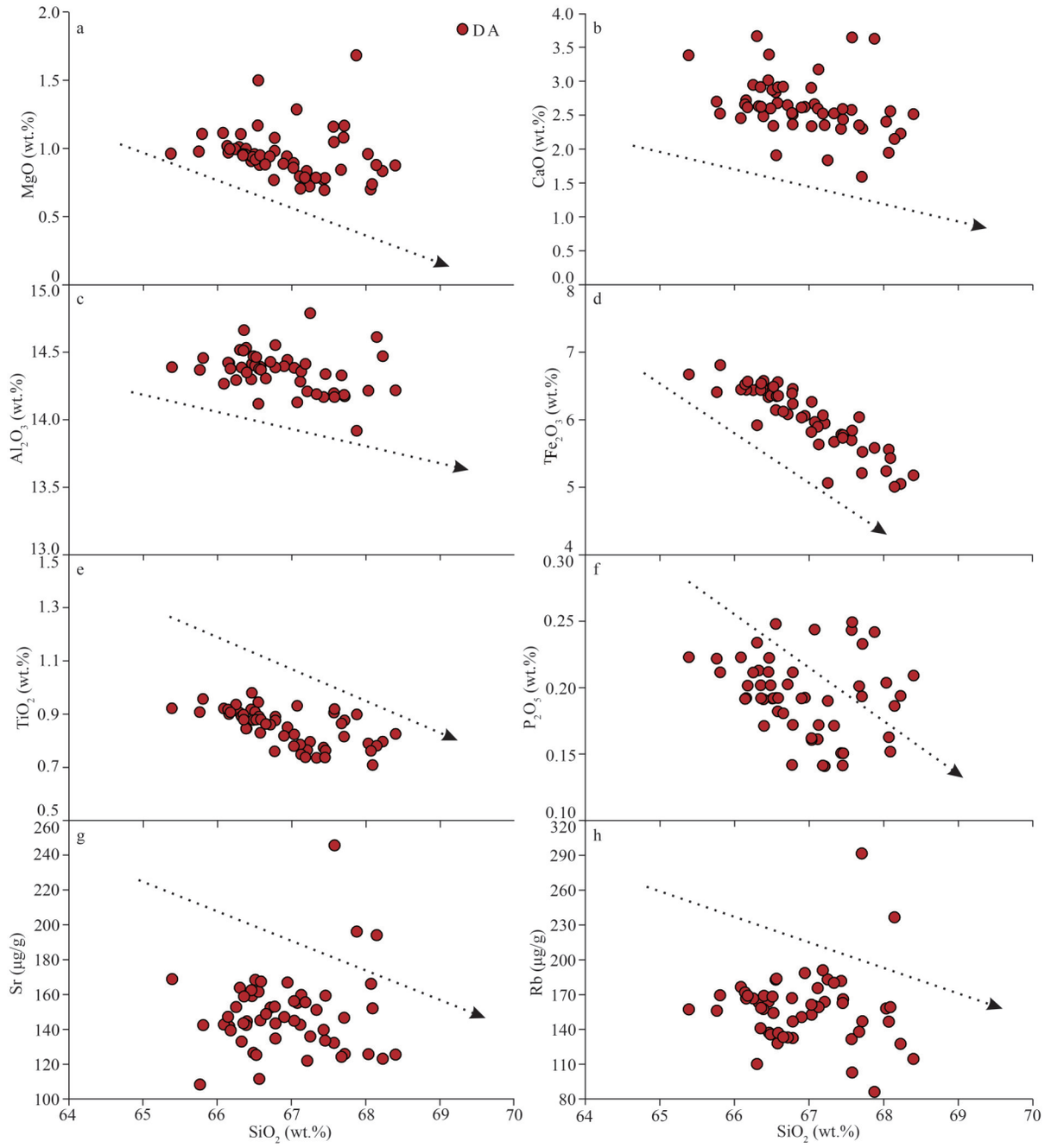

Fig.10 Bivariate plots of selected characteristic components vs. SiO_2 (wt.%) of DA from Well NK-1

Dotted arrows indicate the trend of the data.

upwelling accompanied by a double magma system, forming a rhythmic magma eruption environment.

4.3 Genetic type

4.3.1 Genetic analysis of BA

The BA samples retrieved from Well NK-1 exhibit obvious subduction island-arc calc-alkaline basalt characteristics (Fig.4b), with a flat chondrite-normalized REE pattern (Fig.13a). The BA is more depleted of HFSEs such as Th, U, Ta, and Nb, more enriched by LILEs such as Rb and K than LCC based on the PM-normalized spider diagram (Fig.13b), and has various isotope ratios of $(^{87}Sr/^{86}Sr)_i$ (0.703 77–0.711 18, 0.706 45 on average) and $^{147}Sm/^{144}Nd$ (0.119–0.193, 0.168 on average) (Supplementary Table S5). These characteristics indicate that the magma of the BA source area is relatively enriched in incompatible elements, and

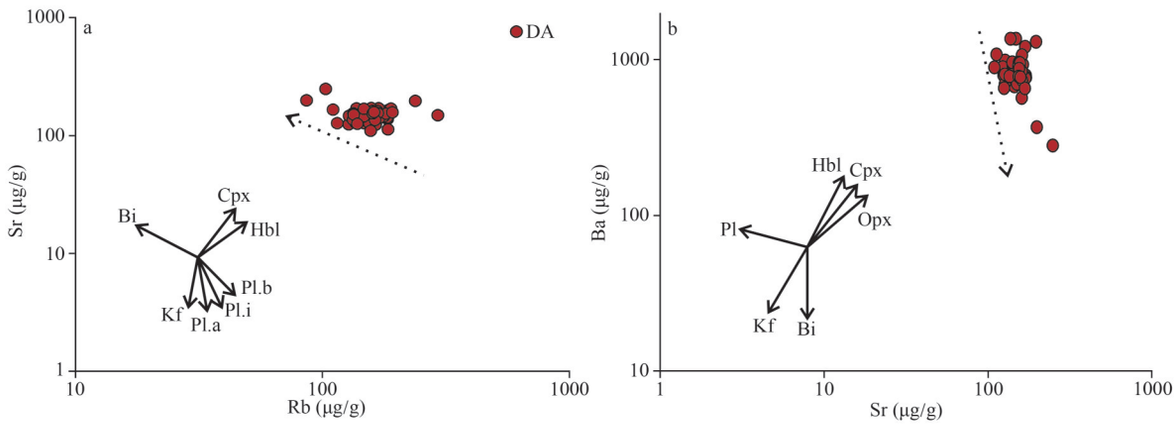

Fig.11 Simulated calculation showing the process of fractional crystallization for Sr (μg/g) vs. Rb (μg/g) (a) and Ba (μg/g) vs. Sr (μg/g) (b) (after Pitcher et al., 1985)

Bi: biotite; Cpx: clinopyroxene; Hbl: hornblende; Kf: K-feldspar; Opx: orthopyroxene; Pl: plagioclase; Pl.a: acid plagioclase; Pl.i: intermediate plagioclase; Pl.b: basic plagioclase. Dotted arrows indicate the trend of fractional crystallization of different minerals.

the material composition of the source area is relatively complex, with the addition of crust-derived characteristic material (Blichert-Toft and Albarède, 1999; Iwamori and Nakamura, 2015).

Several sets of Ta and Nb values are close to or lower than the PM (Fig.13b) without obvious crystallization differentiation of the BA source area that analyzed in Section 4.2.1, which indicates that the initial source area is likely a PM or depleted mantle (DM) (Huang et al., 2013; Li et al., 2018a). The main reason for the enrichment in incompatible elements in BA may be related to the addition of oceanic crust subduction fluid and melt rather than the melting of a typical crust-derived accretionary wedge (Gee et al., 2020). The δCe ($\delta Ce=(Ce_{sample}/Ce_{chondrite})/\sqrt{(La_{sample}/La_{chondrite})\times(Pr_{sample}/Pr_{chondrite})}$) values (0.96–1.04, 1.01 on average) of the BA are lower than those of the UCC (1.11 on average), which indicates that a certain amount of marine sediments may have been trapped during the subduction of the oceanic crust (Singh and Johannes, 1996; Li et al., 2012). Previous studies have shown that these BA magma source characteristics can be caused by arc magmas related to subduction, lithospheric mantle inherited from melt or fluid metasomatism, or contamination from felsic crustal materials (Defant and Drummond, 1990; Hoskin and Schaltegger, 2003). The contamination of felsic crustal materials was first excluded by the nonsignificant contamination from the BA in Section 4.2.1; however, the obvious enrichment of incompatible elements in BA also excludes the possibility of arc magmas related to subduction. The low $(^{87}Sr/^{86}Sr)_i$ ratio (0.703 77–0.711 18, 0.706 45 on average) and the large fluctuation $\varepsilon_{Nd}(t)$ values (-5.7–5.5, 2.7 on average) of the BA (Supplementary Table S5) indicate that the dual influence of mantle- and ancient crust-derived material in the magma chamber was probably caused by the transformation of lithospheric mantle by subduction melt (fluid) (Jahn, 2010; Hong et al., 2017). In Fig.14a, BA samples fall within a triangular pattern between the 10% UCC and 50% LCC margins, indicating that the mixed substances of UCC and LCC are added to the source area. Figure 14b shows that BA samples fall into the upper right of the bulk silicate earth (BSE) point. Both series of rocks show an evolutionary trend toward type EM-II enriched mantle (EM-II), which indicates that the BA source area may not have been affected by a single siliceous and aluminous crustal material. The greater depletion of some elements in BA may not only be the enriched geochemical characteristics of metasomatic lithospheric mantle formation but may also be caused by the magmatic source area originating from PM or DM (Fig.13) (Patiño Douce and Johnston, 1991).

A small number of BA samples were scattered in the mantle plume source region and the normal mid-ocean ridge basalt (N-MORB) and arc magma (ARC) source region boundary, concentrated in the interval between PM and upper crust (UC) (Fig.15a), and showed magma contamination characteristics (Fig.15b). This indicates that the crustal and mantle contamination characteristics of the basic magma chamber in the study area are obvious (Rapp and Watson, 1995). Combined with the fact that the BA (except NK-1-V2-88 and NK-1-

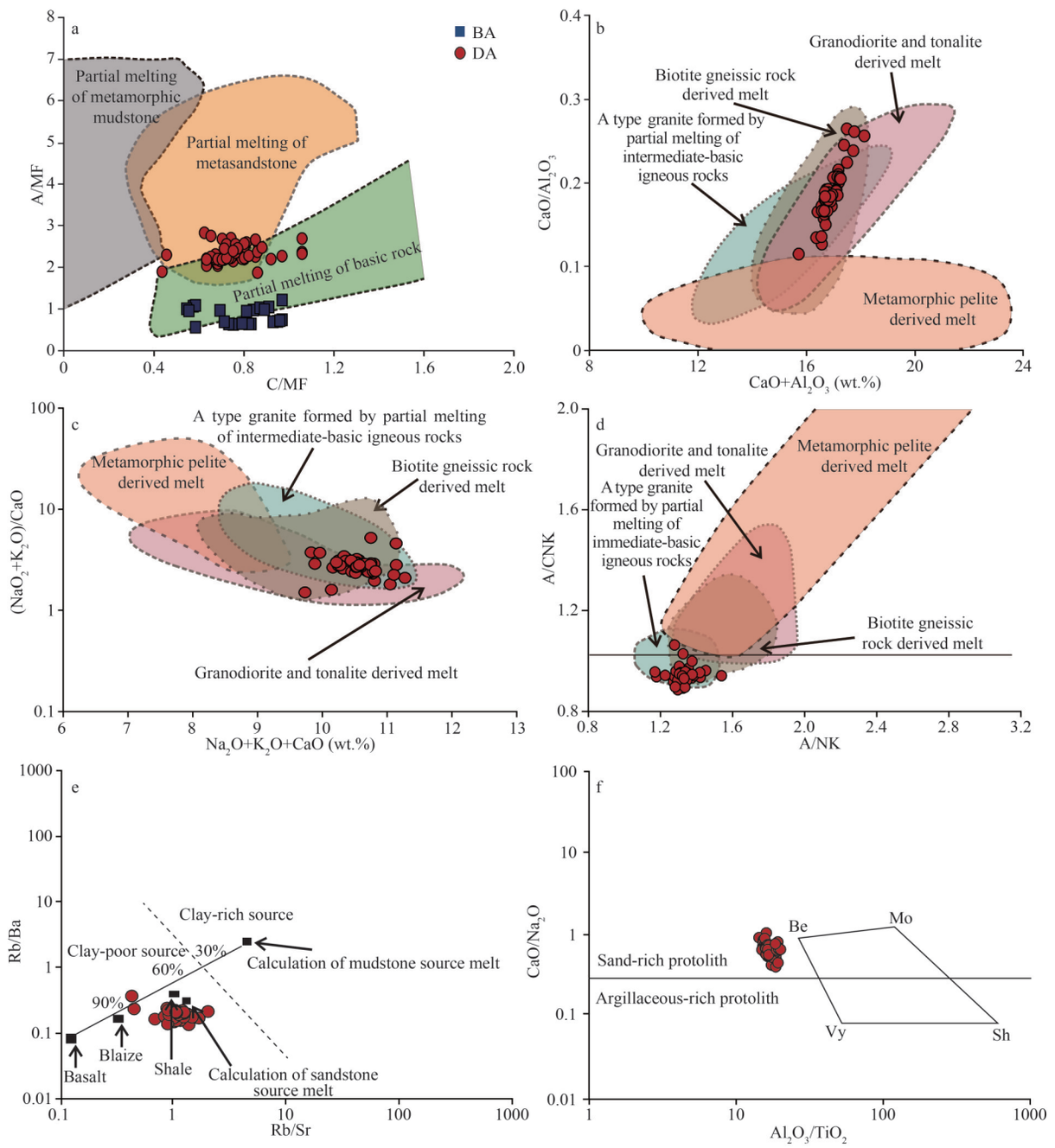

Fig.12 Elemental discrimination diagrams

a. A/MF vs. C/MF (after Altherr et al. (2000)); b. CaO/Al_2O_3 vs. $(CaO+Al_2O_3)$ (wt.%); c. $(Na_2O+K_2O)/CaO$ vs. (Na_2O+K_2O+CaO) (wt.%); d. A/CNK vs. A/NK; e. Rb/Ba vs. Rb/Sr (after Sylvester (1998)); f. CaO/Na_2O vs. Al_2O_3/TiO_2 (after Sylvester (1998)). The data on granodiorite- and tonalite-derived melt are from Patiño Douce (1997), Singh and Johannes (1996), and Skjerlie and Johnston (1993); the data on biotite gneissic rock-derived melt are from Gardien et al. (1995), Patiño Douce (1996), and Patiño Douce and Beard (1995); the data on metamorphic pelitic rock-derived melt are from Gardien et al. (1995), Le Breton and Thompson (1988), Patiño Douce (1996), and Patiño Douce and Johnston (1991); the data on A-type granite formed by partial melting of intermediate-basic igneous rocks are from Feio et al. (2012) and Milani et al. (2015). Be: Bethanga pluton in the Lachlan Fold belt, Australia; Vy: Vysoky-Kamen pluton in Hercynian orogenic belt; Mo: Moschumandl pluton in Alpine orogenic belt; Sh: Shishapangma pluton in Himalayan orogenic belt. A/MF denotes molar $Al_2O_3/(MgO+FeO_{tot})$; C/MF denotes molar $CaO/(MgO+FeO_{tot})$; A/CNK denotes molar $Al_2O_3/(CaO+Na_2O+K_2O)$; A/NK denotes molar $Al_2O_3/(Na_2O+K_2O)$.

V2-79) does not exhibit positive Zr and Hf anomalies, it is suggested that the assimilation and contamination during magma upwelling should be weak, and the element enrichment and crust-mantle contamination characteristics are derived from the magma chamber properties in the source region. The

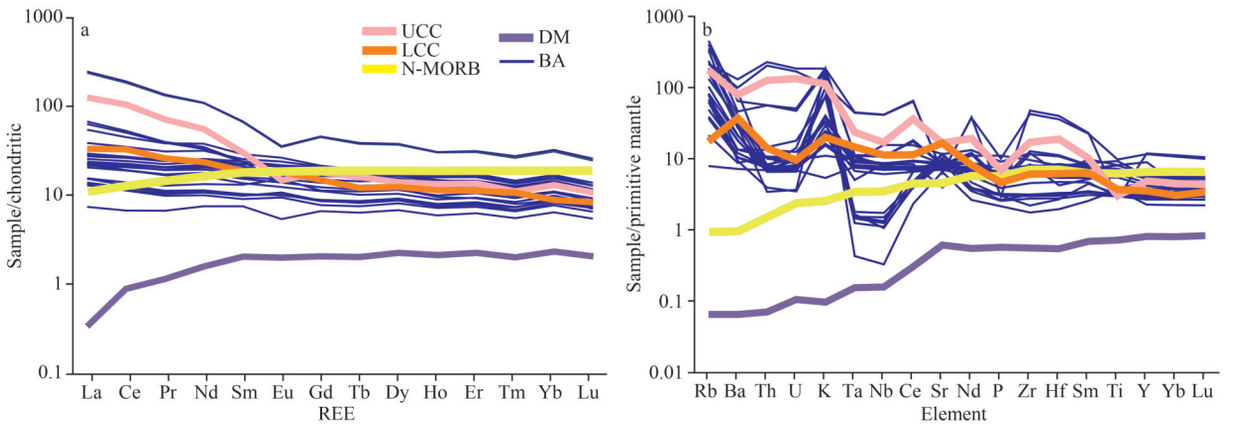

Fig.13 The chondrite-normalized REE distribution pattern of the BA (a) and the primitive mantle-normalized spider diagram of the BA (b) (normalized after Sun and McDonough (1989))

UCC (upper continental crust), LCC (lower continental crust), N-MORB (normalized mid-ocean ridge basalt), and DM (depleted mantle) data are from Taylor and McLennan (1985).

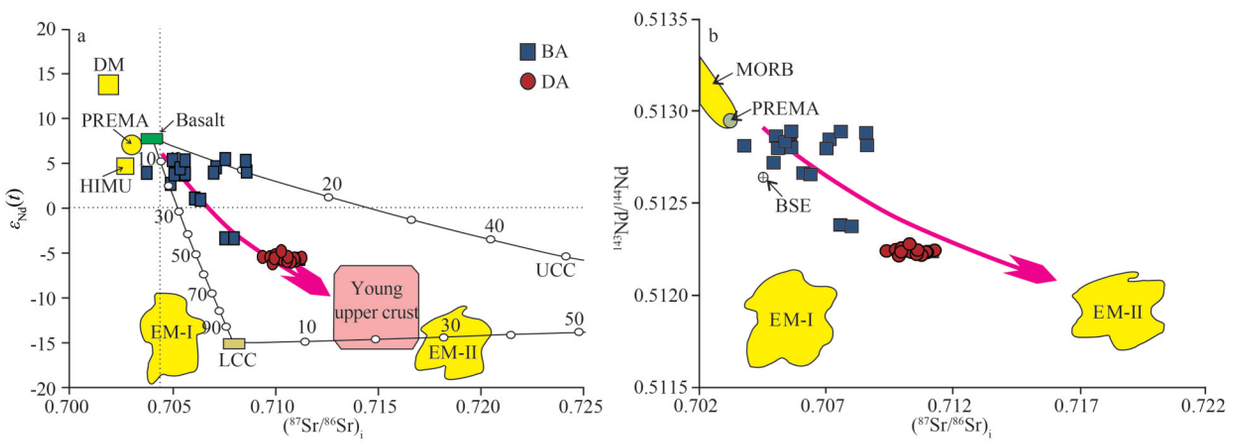

Fig.14 Discrimination diagrams of $\varepsilon_{Nd}(t)$ vs. $(^{87}Sr/^{86}Sr)_i$ (after Zindler and Hart (1986)) (a) and $^{143}Nd/^{144}Nd$ vs. $(^{87}Sr/^{86}Sr)_i$ (after Zindler and Hart (1986)) (b)

BSE: bulk silicate earth; DM: depleted mantle; EM-I: EM-I enriched mantle; EM-II: EM-II enriched mantle; HIMU: high $^{238}U/^{204}Pb$; LCC: lower continental crust; MORB: mid-ocean ridge basalt; PREMA: prevalent mantle; UCC: upper continental crust; they are from Zindler and Hart (1986).

BA has the characteristics of typical subducted island-arc volcanic rocks (Fig.15c). In Fig.15d, BA data fall into the oceanic island-arc range affected by the volcanic arc and the calc-alkaline basalt region transitive to the active continental margin. Combined with the trend consistent with the evolution of the intraoceanic arc (Fig.15e), it is suggested that the BA should be a mature island-arc volcanic rock, and its forming environment is biased to the side of the continental margin of the intraoceanic arc, with obvious continental crust pollution attributes (Fig.15f). It is worth noting that although NK-1-V2-193, NK-1-V2-79, and NK-1-V2-88 samples in BA obviously have high Nb content (up to 29.66 μg/g), their Zr and Hf enrichment trends are not obvious, which is different from previous studies of Nb-rich basalts. The analysis (Fig.16a–b) shows that the overall data fall into the normal arc magma field, showing the characteristics of classical island-arc magmatic rocks, which indicates that the enrichment of incompatible elements in BA is more likely caused by the fluid or melt formed by the continental crust accretionary wedge accompanied by oceanic crust subduction (Zhao et al., 2016; Yu et al., 2020).

Based on the above characteristics, it is concluded that the BA features obvious properties of subduction zone composition (SZC), and the EM-II characteristics shown by Sr-Nd isotope data indicate that the magma source area may be influenced by crust-mantle contamination (e.g., subducted recirculating sediments, recirculating oceanic crust, and SCLM) (Huang et al., 2013; Gee et al., 2020). According to the petrological characteristics in Section 3.2, the

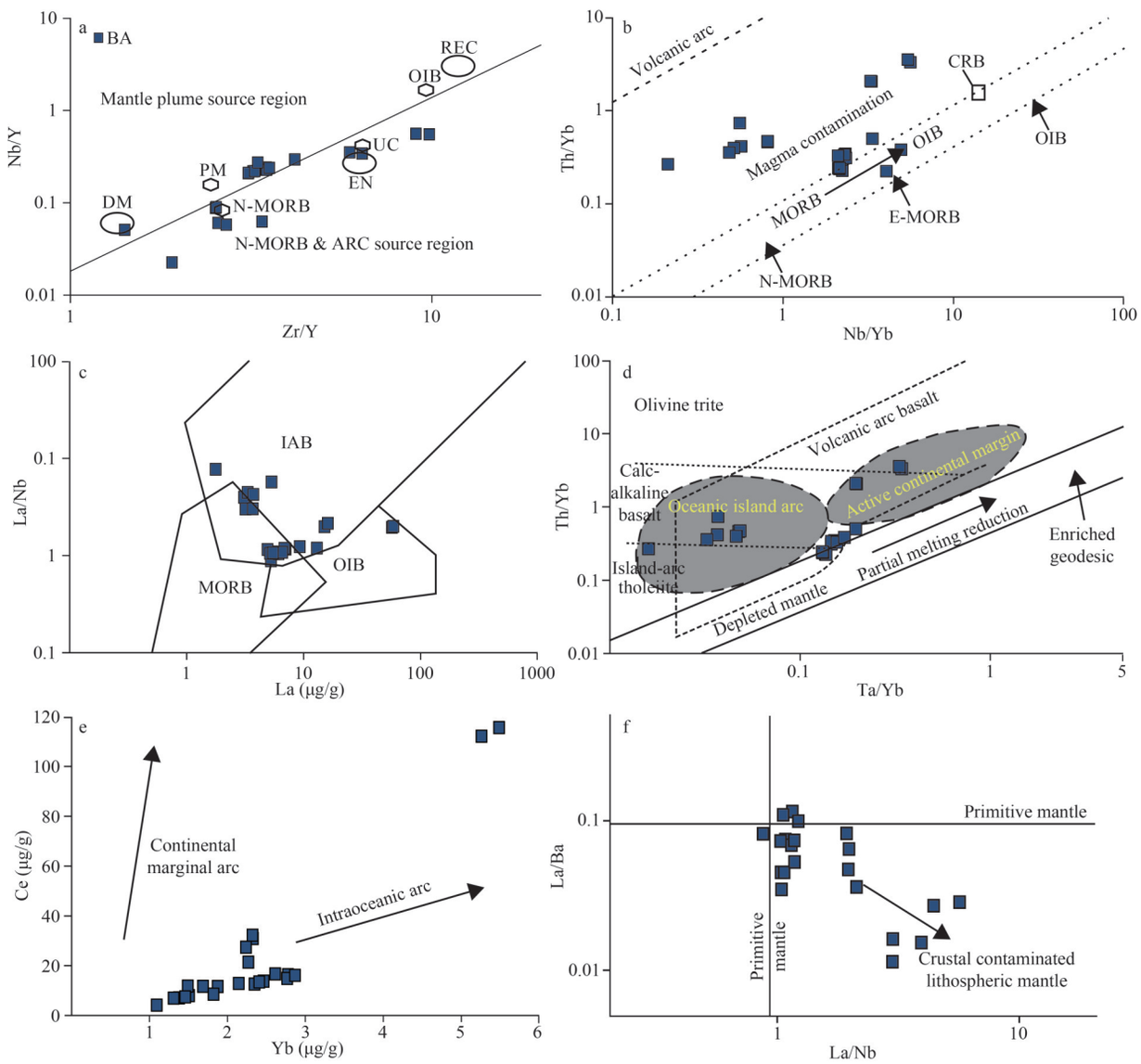

Fig.15 Discrimination diagrams of Nb/Y vs. Zr/Y (after Fitton et al. (1997)) (a); Th/Yb vs. Nb/Yb (after Pearce (2008)) (b); La/Nb vs. La (μg/g) (after Wang et al. (2019)) (c); Th/Yb vs. Ta/Yb (after Pearce (1982)) (d); Ce (μg/g) vs. Yb (μg/g) (after Stevenson (2018)) (e); and La/Ba vs. La/Nb (after Miller et al. (1999)) (f)

ARC: arc magma; CRB: continental rift basalt; DM: depleted mantle; E-MORB: enriched mid-ocean ridge basalt; EN: enriched mantle; IAB: island arc basalt; MORB: mid-ocean ridge basalt; N-MORB: normal mid-ocean ridge basalt; OIB: oceanic island basalt; REC: recycling plant composition; UC: upper crust.

BA has a relatively euhedral to subhedral mafic hydrous amphibole, which suggests that it may be related to the water-bearing fluid derived from the subducted plate. According to the discrimination of Ba/Th-La/Sm (Fig.17a), the BA has a high coupling with subduction plate dehydration and a high oxygen fugacity trend. Combined with the influence of fluid metasomatism shown by the BA in Fig.17b, it can be concluded that the source area of the BA obviously experienced fluid metasomatism after dehydration of subducted plate. Ta^* and Nb^* can be used as criteria to distinguish the mantle-derived characteristics of basalts. In the Ta^* vs. Nb^* diagram (Fig.17c), BA samples are mainly located near the PM and below the average continental crust (ACC), showing obvious clustering. One set of data suggests the addition of continental crust material, while the other set of data indicates that the primitive magma should have derived from the PM. Further input of BA data into $[Hf/Sm]_{PM}$-$[Ta/La]_{PM}$ discrimination (Fig.17d) shows that the samples basically plot in the subduction metasomatism field, showing the characteristics of the source area influenced by both subduction melt and fluid. In

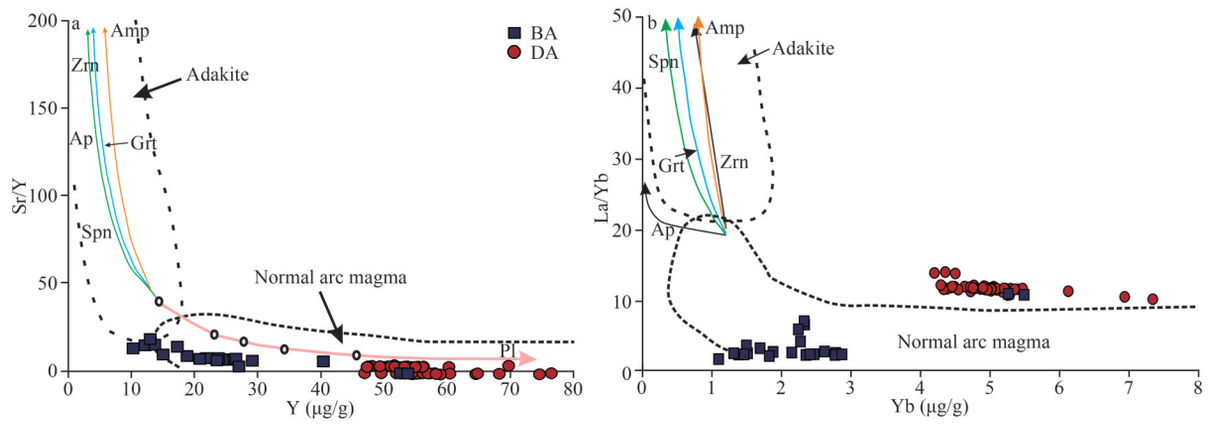

Fig.16 Plots of Sr/Y vs. Y (μg/g) (after Defant and Drummond (1990)) (a) and La/Yb vs. Yb (μg/g) (after Defant and Drummond (1990)) (b)

Amp: amphibole; Ap: apatite; Zrn: zircon; Grt: garnet; Spn: spinel; Pl: plagioclase.

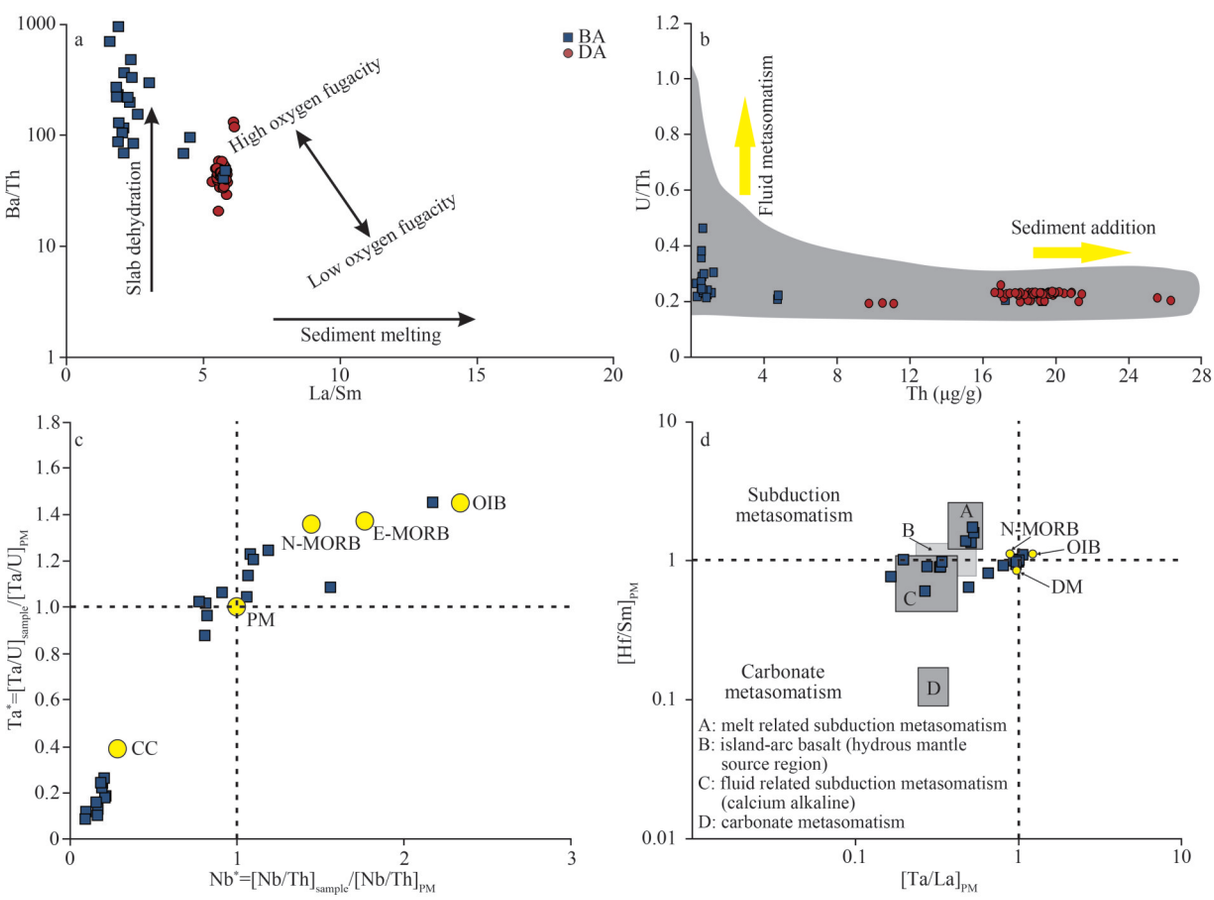

Fig.17 Plots of Ba/Th vs. La/Sm (after Labanieh et al. (2012) and Li et al. (2022)) (a); U/Th vs. Th (μg/g) (after Sun et al. (2003)) (b); Ta^* vs. Nb^* (after Pearce et al. (2005)) (c); and $[Hf/Sm]_{PM}$ vs. $[Ta/La]_{PM}$ (after Pearce et al. (2005)) (d)

CC: continental crust.

conclusion, the melt (fluid) produced by the subduction of crust-derived sediments wrapped by oceanic plates may be the main factor leading to water-, volatile matter- and incompatible element-rich conditions in the BA source area.

4.3.2 Genetic analysis of DA

The chondrite-normalized REE pattern of the DA (Fig.8a) shows a gentle right-leaning pattern, with more enrichment of ΣREE (245.49–376.16 μg/g, with an average value of 284.36 μg/g) than those of UCC, a

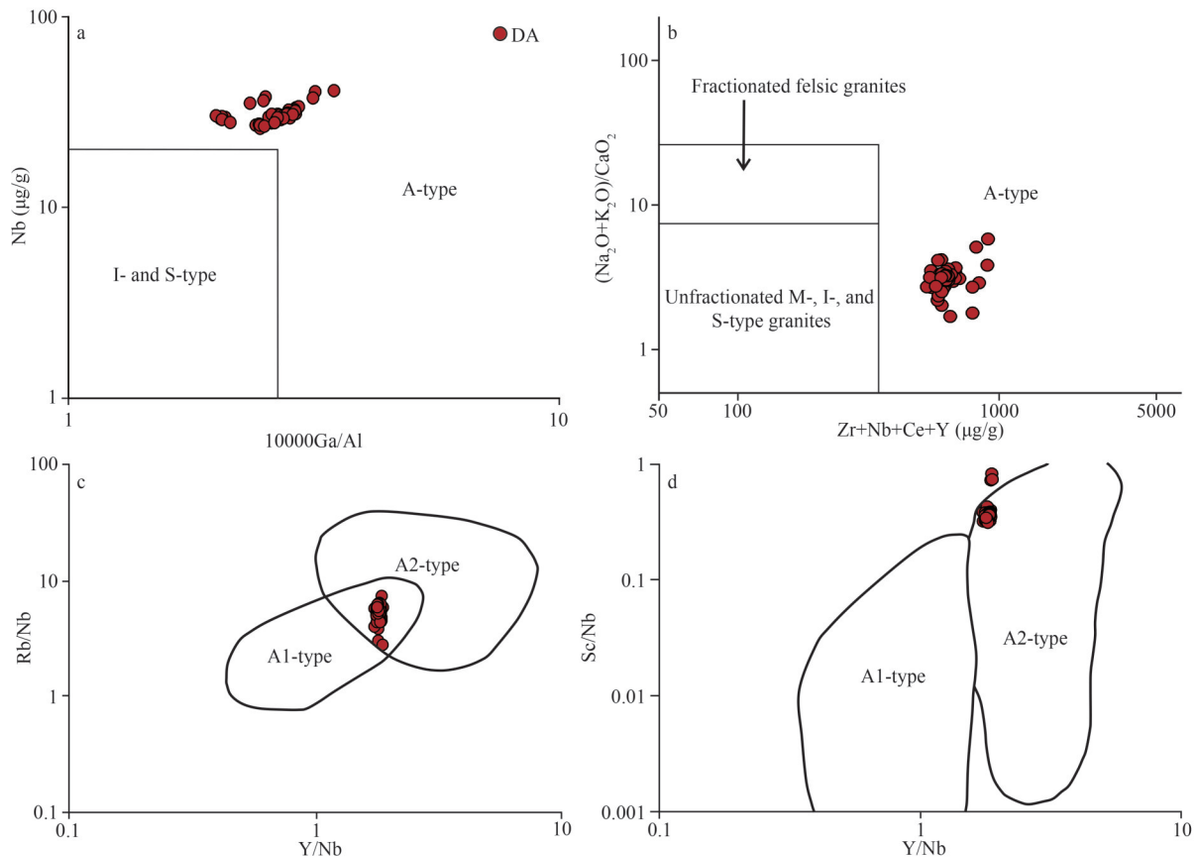

Fig.18 Nb (μg/g) vs. 10000Ga/Al diagram (after Whalen et al. (1987)) (a); $(Na_2O+K_2O)/CaO$ vs. (Zr+Nb+Ce+Y) (μg/g) diagram (after Whalen et al. (1987)) (b); Rb/Nb vs. Y/Nb diagram (after Eby (1992)) (c) and Sc/Nb vs. Y/Nb diagram (after Eby (1990)) (d)

slight positive δCe anomaly (1.01–1.07, 1.04 on average), a moderate negative δEu ($\delta Eu = (Eu_{sample}/Eu_{chondrite})/\sqrt{(Sm_{sample}/Sm_{chondrite}) \times (Gd_{sample}/Gd_{chondrite})}$) anomaly (0.60–0.70, 0.63 on average), and a high LREE/HREE ratio (2.40–2.92, 2.81 on average). The PM-normalized spider diagram (Fig.8b) shows curve characteristics similar to those of the UCC, with significant enrichments in LILEs Rb and K and HFSEs Th, U, Zr, Hf and REEs and depletions in LILEs Ba, Sr, and P and HFSEs Ta, Nb, and Ti, which shows significant geochemical characteristics of siliceous and aluminous crust. DA rocks have the characteristics of A-type granite (Fig.18a–b), which may derive from the alkali-rich magma source area (Patiño Douce, 1997; Feio et al., 2012). Figure 18c–d shows that DA data basically plot into the A2-type region, suggesting that the magma source area of DA may have formed in a thinning crustal environment. However, there are some differences between DA and the traditional A-type granites in the "wing-type" distribution of the chondrite-normalized REE pattern, enrichment in Yb and K_2O and strong negative δEu anomalies. The Nb/U ratio of DA (7.67 on average) is lower than that of MORB (47 on average) and that of the average crust (10 on average); and the Ce/Pb ratio of DA (2.62–8.50, 5.10 on average) is similar to that of ACC, indicating the addition of a certain mantle source material. Combined with the data of DA samples falling in the normal arc magma field (Fig.16a–b) and similar characteristics of island-arc Zhejiang and Fujian granites (Zhang et al., 2010) (characterized by moderate negative δEu anomalies, Sr content and Yb content varying in 30–400 μg/g and 1–7 μg/g, respectively), it can be concluded that the magma source area of DA is a typical subducted island-arc andesitic magma produced in an environment of crustal thinning (Stevenson, 2018). The high $(^{87}Sr/^{86}Sr)_i$ ratio of DA (0.709 39–0.711 29, 0.710 35 on average), the less varied $\varepsilon_{Nd}(t)$ values (-6.2–-4.8, -5.6 on average) and $\varepsilon_{Hf}(t)$ values (-2.9–-1.7, -2.2 on average) (Supplementary Table S5), the isotopic values close to the young UC (Fig.14a) and

the evolutionary trend toward EM-II (Fig.14b) suggest that the magma source area was the product of partial melting of the lower crust, the magma chamber environment was relatively closed, and the element enrichment attribute was the result of the evolution of magma differentiation and crystallization (Li et al., 2009).

According to the analysis of the Harker diagram (Fig.10) and source area discrimination diagram (Fig.12), DA rocks have the characteristics of obvious mafic magma melting or biotite gneiss-derived melt, and the obvious crystallization differentiation attribute indicates that DA should be derived from the location of the lower crust and lithospheric mantle. Further analysis of the Pb isotope characteristics of DA shows that the data plot close to the EM-II region (Fig.19a–b), showing obvious crust-mantle metasomatism. Combined with the EM-II characteristics of DA in Fig.14, both suggest that the subduction of the western Pacific resulted in continuous asthenospheric underplating on the continental margin, and partial melting of the lithospheric mantle and lower crust formed the magma chamber in the DA source area. DA is highly similar to the Triassic granites of the SCC in isotopic geochemistry, which indicates an affinity between the Meiji Reef and SCC (Jahn, 2010; Li et al., 2018a; Hou et al., 2019).

Based on the analysis of rock geochemistry and isotopic geochemistry of BA and DA, the overall lithology changed gradually from the bottom of DA to the top of BA and DA alternately, with good continuity in the core feature. This may imply that the continuous fractional crystallization of pyroxene and olivine in the basic magma produced a large amount of silicate unsaturated alkaline melt, resulting in more obvious alkaline characteristics of the upper cycle.

The large fluctuations $\varepsilon_{Hf}(t)$ values (-1.5–11.5, 5.7 on average) and T_{DM}(Ma) ages (808–3 434 Ma, 1 415 Ma on average) larger than zircon U-Pb ages in BA, and the relatively stable $\varepsilon_{Hf}(t)$ values (-1.7–-2.9, -2.2 on average) and T_{DM} (Ma) age (1 128–1 238 Ma, 1 162 Ma on average) larger than zircon U-Pb age in DA (Supplementary Tables S4–S5), suggesting that a portion of crust-derived accretionary wedge wrapped by subduction in the western Pacific Ocean entered deep, a large number of subduction melt (fluid) formed with the intensification of subduction depth were rapidly added to the asthenosphere, forming enrichment mantle-derived magma chamber (EM-II-typed) of the BA in the study area. As asthenospheric upwelling continued to underplate, the DA source magma chamber was formed by partial melting of the lithospheric mantle and lower crust, and the upwelling of magma intensified the gradual thinning of the crust on the continental margin. Subsequently, tectonic fractures appeared, and then the magma chamber in the DA source area was the first to erupt; magma from the deeper BA source area also rapidly erupted to form rocks along this conduit. The rhythmic interbedding revealed by the petrographic analysis also confirmed this view. BA and DA show a trend of decreasing $\varepsilon_{Hf}(t)$ values with the age of T_{DM} (Ma), and the correlation is high in Fig.20a, which also indicates that the BA was influenced by obvious new crust, while DA received more ancient

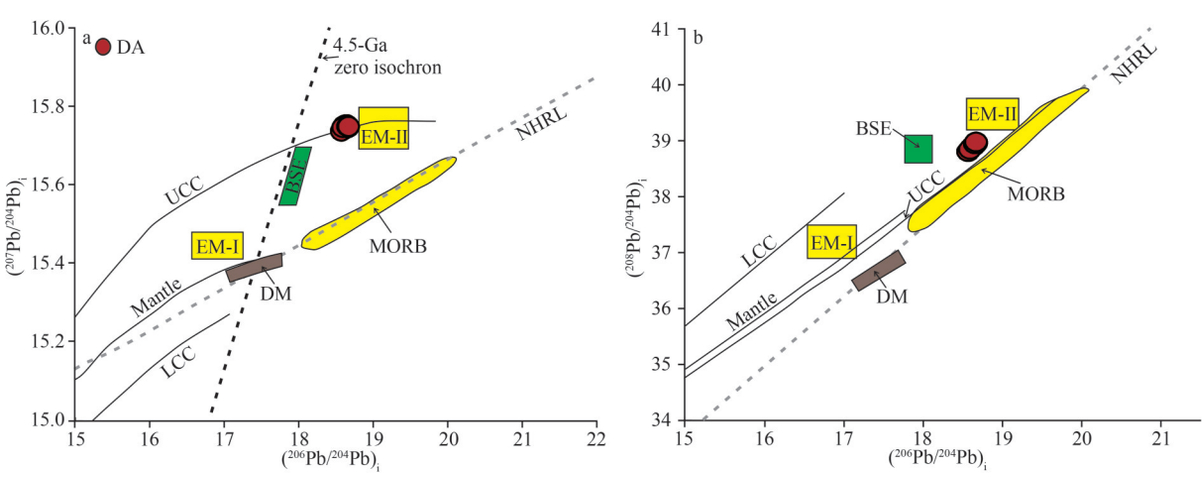

Fig.19 $(^{207}Pb/^{204}Pb)_i$ vs. $(^{206}Pb/^{204}Pb)_i$ diagram (after Zindler and Hart (1986)) (a); and $(^{208}Pb/^{204}Pb)_i$ vs. $(^{206}Pb/^{204}Pb)_i$ diagram (after Zindler and Hart (1986)) (b)

NHRL: northern hemisphere reference line.

crust-derived materials (Fig.20b). However, the two samples with older model ages in BA indicate the addition of ancient crust-derived materials at the same time (Blichert-Toft and Albarède, 1999).

4.4 Tectonic spatio-temporal attribute

In addition to the eruption and overflow facies, the cryptoexplosive breccia facies appeared in the upper 1 315.3–1 292.5 m in the petrographic characteristics of the core samples from Well NK-1 of the Meiji Reef, indicating that the volcanic rock layer was thickly accumulated at this time and rich in fluid or gas components, resulting in magma emplacement to a shallow place and pressure eruption. According to the research results of Valentine et al. (2014), the depth of magma eruption at this time was relatively shallow (<200 m) and there was some water environment interference. Their results are not only consistent with the microscopy identification results but also suggest that the magma eruption at this time occurred in a relatively open (extension and relaxation) environment. The lenticular welded tuff bands developed at 1 275.2 m, indicate that the volcanic eruption environment in the study area was already in the aquatic environment. The limited potassization, slight silicification, and late carbonation in the first-cycle core samples also indicate that the magma in the source region transformed into alkaline and volatile components, suggesting that the tectonic environment in the study area is only equivalent to the early stage of extrusion to tension transformation (Caricchi et al., 2014).

According to zircon U-Pb geochronology analysis of DA samples from 1 225.4 to 1 684.0 m in cores (Supplementary Table S4; Miao et al., 2021; Wei et al., 2022), the age of volcanic rocks in the Meiji Reef ranges from 218.6±3.2 Ma to 217.9±3.5 Ma. Because DA and BA were interbedded without obvious alteration, it is believed that DA and BA were the products of the magmatic eruption at the same time. The analysis of the tectonic environment of the DA rocks (Figs.21–22) shows that the DA volcanic rocks of the Meiji Reef should have been produced in the initial back-arc region of the subduction zone, and the tectonic environment was the transitional stage from extrusion to extension.

Based on the analysis of the tectonic environment of the BA (Fig.23) and the characteristics of the extensional environment on the terrigenous side shown by DA, it is concluded that the BA-produced environment of the Meiji Reef was a subduction arc-back initial extensional basin. Combined with the extrusion-extension transition characteristics of DA in the study area, it is concluded that the overall tectonic environment of the Meiji Reef in the Late Triassic was more likely produced by the initial extensional environment (initial continental margin extensional rift environment) under the relative extrusion environment than the obvious back-arc extension characteristics (Meschede, 1986). This interpretation is consistent with the accordion-type periodic “open-close” dynamic background proposed by Yang et al. (2002), which is dominated by extensional tectonics, indicating that the magma production environment in the study area is a dynamic rhythmic change rather than an example of simple extensional tectonics. This interpretation is also consistent with the complex tectonic and geological background of the ancient continent in South China.

4.5 Mechanism of subduction on the western side of the ancient Pacific Ocean

The SCC was affected by the Paleo-Pacific subduction during the Triassic period, but the study of subduction arc magmatic rocks during this period

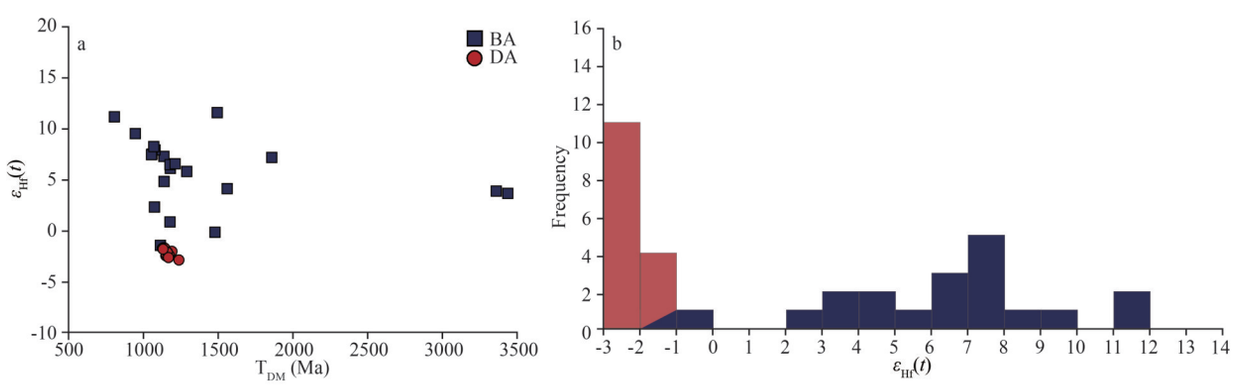

Fig.20 $\varepsilon_{Hf}(t)$ vs. T_{DM} (Ma) diagram (a) and $\varepsilon_{Hf}(t)$ frequency histogram (b) of volcanic rocks from Well NK-1

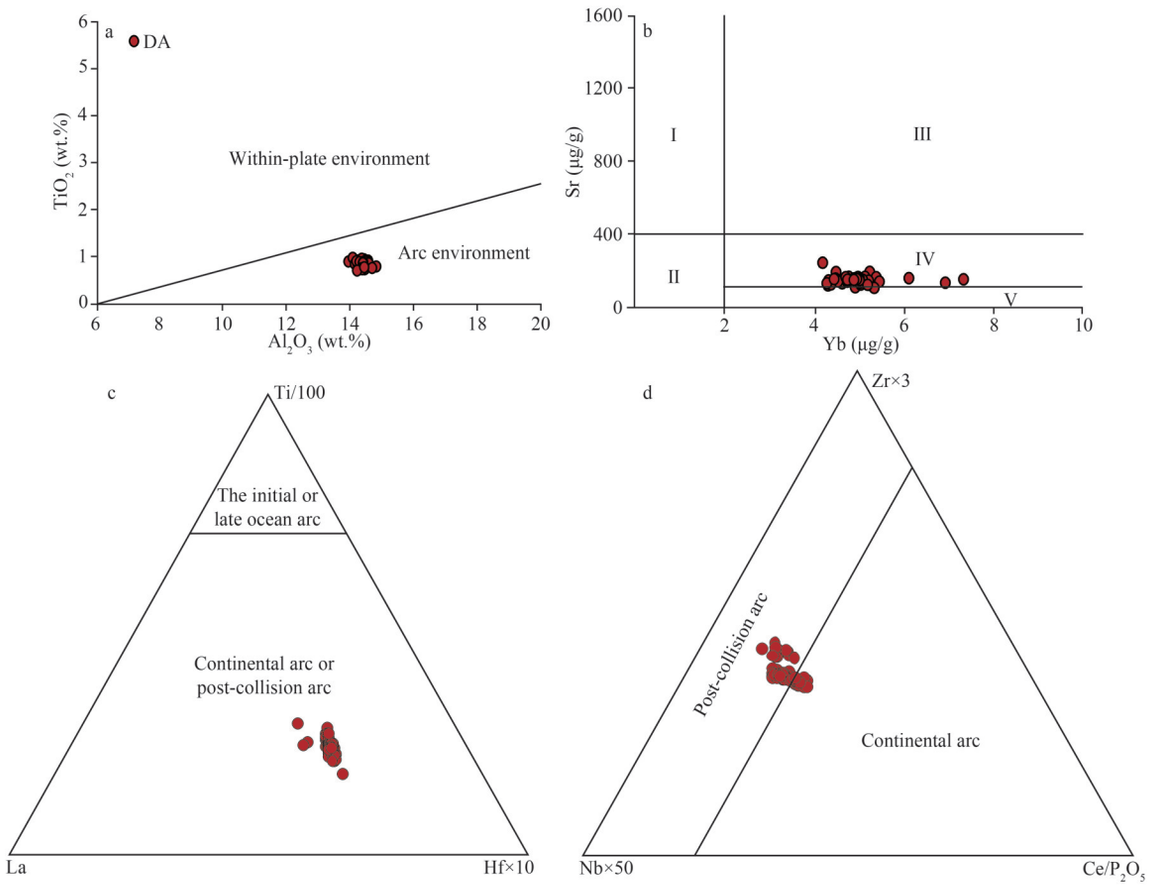

Fig.21 TiO_2 (wt.%) vs. Al_2O_3 (wt.%) diagram (after Müller and Groves (2000)) (a); Sr (μg/g) vs. Yb (μg/g) diagram (after Kong et al. (2012)) (b); Ti/100 vs. La vs. Hf×10 ternary diagram (after Müller and Groves (2000)) (c); and Zr×3 vs. Nb×50 vs. Ce/P_2O_5 ternary diagram (after Müller and Groves (2000)) (d)

I: granite with high Sr and low Yb values (adakite); II: granite with low Sr and high Yb values (Himalaya-type granite); III: granite with high Sr and high Yb values; IV: granite with low Sr and high Yb values (Fujian- and Zhejiang-typed granite); V: granite with very low Sr and high Yb values (Nanling-typed granite).

is obviously lacking, which makes the mechanism of Paleo-Pacific subduction controversial. The U-Pb isotopic geochronology data of volcanic rocks from Well NK-1 of the Meiji Reef in this paper show that magmatic eruptions occurred in the early Late Triassic, which provides important subduction time nodes and deep geochemical field data for the study of the ocean-continental transition zone between the SCC and the Western Pacific. The BA in the study area shows the magmatic characteristics of subducted island arcs with multisource properties, and subduction components should be added to the mantle wedge (Fig.14). Some previous studies attributed the changes in geochemical dynamics in the subduction zone to the mixture of three components, namely, DM, sediment melt, and aqueous fluid generated by dehydration of altered ocean crust (Patiño Douce, 1996). The enrichment of LILEs (such as Ba and Sr) and LREEs (such as La, Ce, and Nd) in arc magma has been confirmed by rock simulation experiments, as mainly caused by subduction components added to the mantle wedge (Patiño Douce and Beard, 1995). The content of Ba and Sr in BA is significantly higher than that of PM in the study area, indicating that there should be an obvious subduction component in the source area, which is closely related to subduction melt (fluid). According to the core depth (age) and multi-element and isotope geochemical analysis in Fig.24, the zircon U-Pb ages are basically the same (220.5–215 Ma), indicating that the volcanic rocks with a thickness of nearly 1 000 m should have been formed in a simultaneous eruption. In addition, the BA data in Fig.24 show significant fluctuations with the depth of the well column, especially the significantly fluctuating Ti/Ti^* curve, which indicates that the BA source area is affected by both recirculating oceanic crust and recirculating sediments. In addition, the

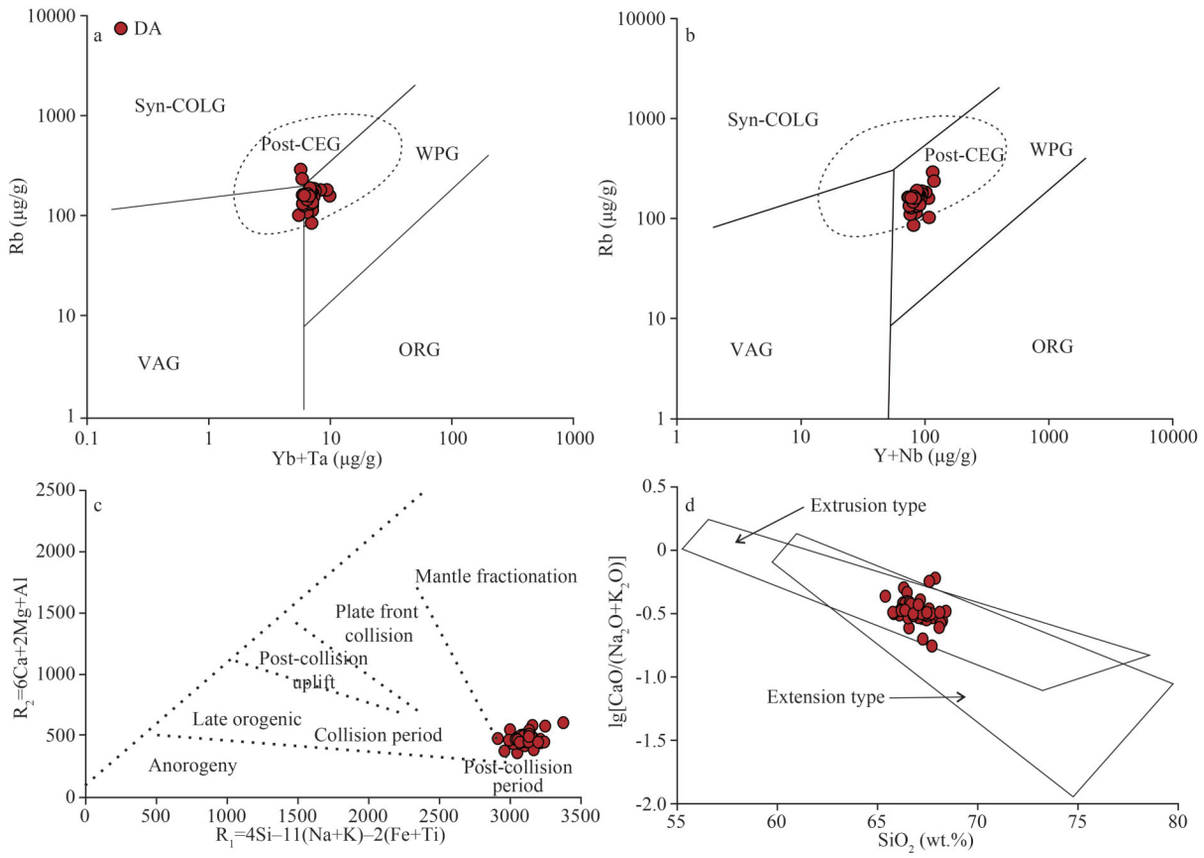

Fig.22 Distribution of the volcanic rock data retrieved from Well NK-1 in Rb (μg/g) vs. (Yb+Ta) (μg/g) (a) and Rb (μg/g) vs. (Y+Nb) (μg/g) discrimination diagrams of Pearce et al. (1984) (b); R_2 vs. R_1 diagram (after Batchelor and Bowden (1985) (c) and lg[CaO/(Na_2O+K_2O)] vs. SiO_2 (wt.%) diagram (after Maniar and Piccoli (1989) (d)

Syn-COLG: syn-collision granites; post-CEG: post-collision extensional granites; VAG: volcanic arc granites; WPG: within plate granites; ORG: ocean ridge granites.

ratios of Nd/Sr and Ba/La in BA show the characteristics of sharp fluctuations at the same location (1 400–1 450 m and 1 200–1 300 m), indicating that the subduction material composition decreased first and then intensified during the eruption process. The consistent geochemical data characteristics of DA again indicate a stable and relatively closed environment in the source area.

The obvious fluctuation data characteristics of the BA suggest the complexity of the source area. The tholeiitic index (THI) of the BA is 0.705, calculated using the THI proposed by Zimmer et al. (2010), which represents the relative depletion of FeO in magma. It should be the calc-alkaline magma series, which is consistent with the calculation range of global island-arc basalt. In the SiO_2-TFeO/MgO diagram of Hora et al. (2009) (Fig.25), BA data mostly fall into the tholeiitic region below the CA (calc-alkaline)/TH (tholeiitic) index=1 line and are in the range of medium-Fe to high-Fe transitions, which is consistent with the global data of MORB and backarc basin basalt (BABB) and is in the primary stage of MORB and BABB evolution. However, it is worth noting that the obvious island-arc basalt (IAB) imprint of the BA geochemical properties may not support the true sense of MORB and BABB. This indicates that the BA has calc-alkaline island-arc properties and develops into intraplate tholeiite. Combined with the calc-alkaline characteristics of the BA geochemical characteristics shown above, it is believed that it belongs to the late stage of island-arc magmatic development and has obvious mature island-arc characteristics, but it is different from the basalt of the back-arc basin and should be the product of early-stage back-arc extension. The study of global magma data showed that THI formed a very obvious inverse correlation with H_2O, and the increase in water content in magma dominated the transition from calc-alkaline to intraplate tholeiitic magma. Furthermore, using

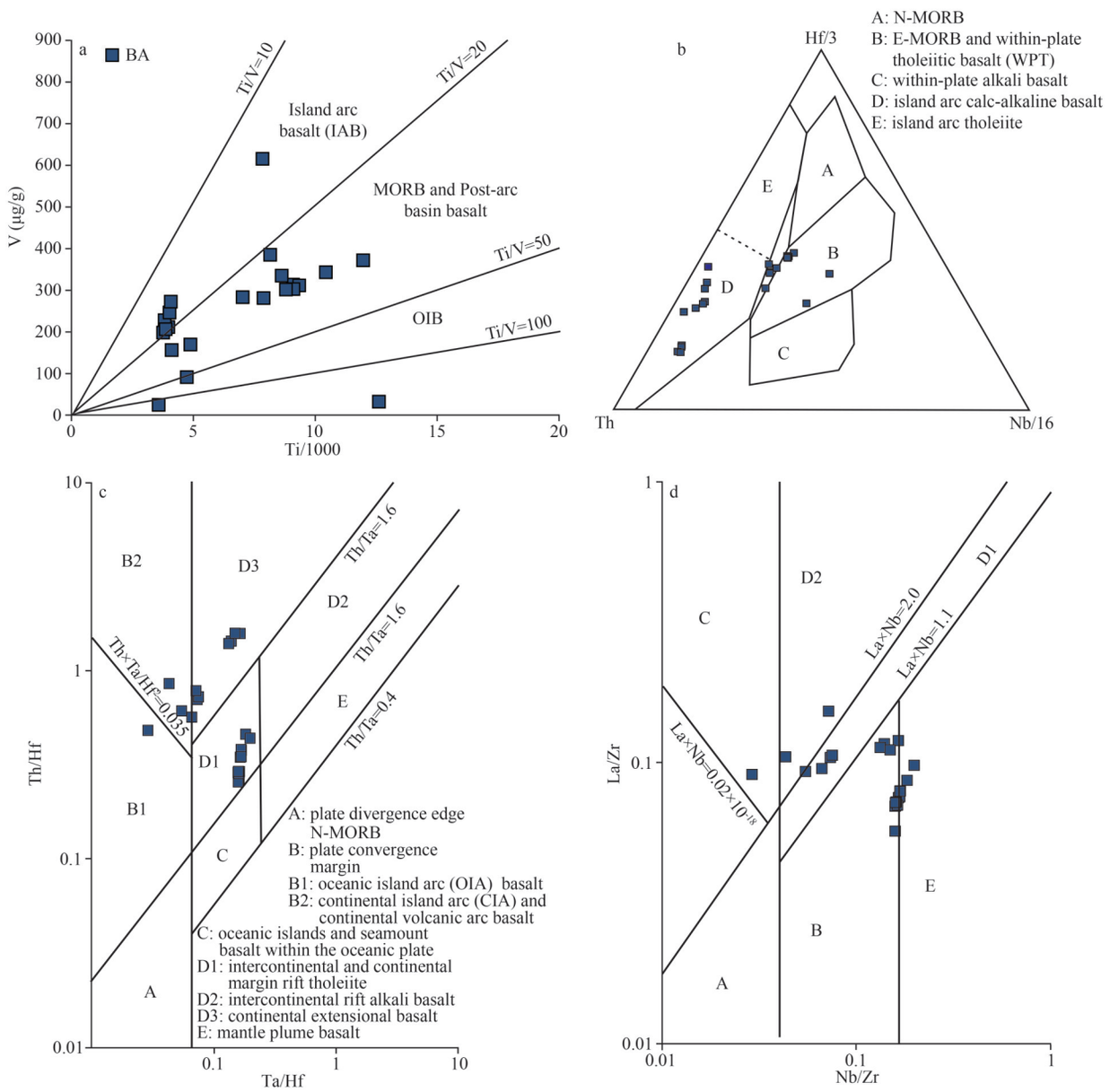

Fig.23 V (μg/g) vs. Ti/1 000 diagram (after Pearce and Cann (1973) and Shervais (1982)) (a); Hf/3 vs. Th vs. Nb/16 ternary diagram (after Wood (1980)) (b); Th/Hf vs. Ta/Hf diagram (after Wang and Li (2001)) (c) and La/Zr vs. Nb/Zr diagram (after Wu et al. (2003)) (d)

the H_2O content calculation formulas of Zimmer et al. (2010) and Kelley et al. (2010), the BA magmatic water content is 5.7 wt.% and 5.6 wt.%, respectively. The results are consistent in general with the evolution trend of the liquid lines of descent. The study of Tollan and Hermann (2019) showed that the dehydration effect of the subducted slab could form island-arc magmas with water-rich phases and high oxygen fugacity, which can metasomatize the overlying continental mantle wedge. However, H_2O in aqueous solution can further produce H_2 and O_2, which makes the mantle source more oxidized.

Based on this analysis and previous studies on the subduction model of the western side of the Paleo-Pacific Ocean, it is concluded that the Meiji Reef underwent obvious Pacific Plate slab subduction during the Late Triassic. A large number of previous studies have found that a large amount of terrigenous accretionary wedge material can be wrapped by oceanic plate subduction into the deep asthenosphere to form recirculating sediment melt (Turner et al., 2000; Yan et al., 2020); however, the

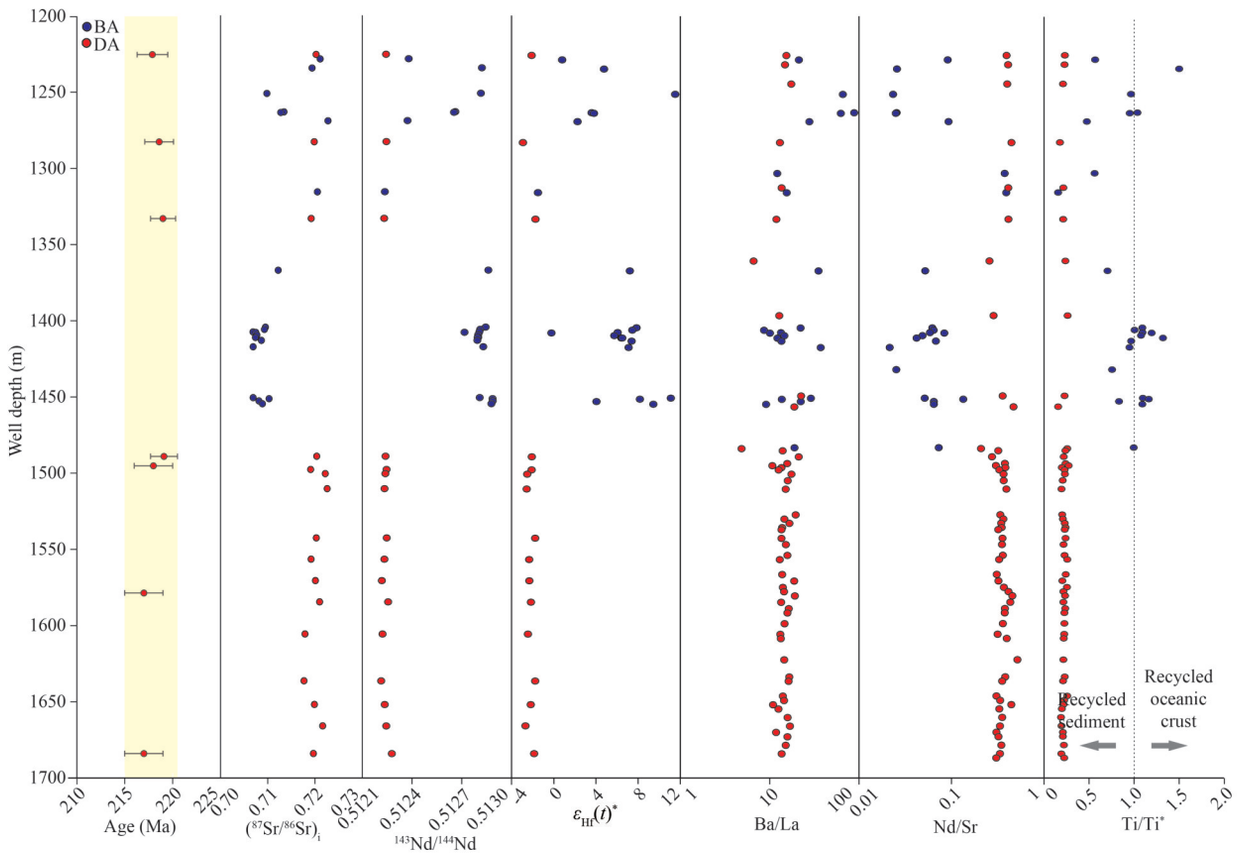

Fig.24 The relationship between core depth and age and multi-element and isotopic geochemistry from Well NK-1

The yellow area represents the age range.

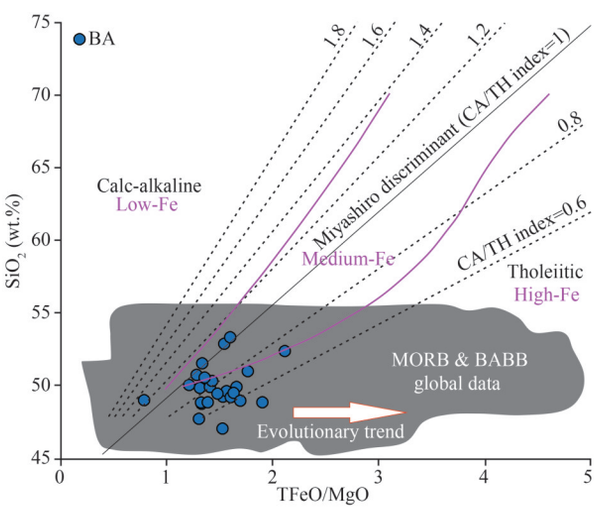

Fig.25 SiO_2 (wt.%) vs. TFeO/MgO plot (after Arculus (2004))

oceanic crust can also form recirculating oceanic crust melt (Wang et al., 2002). Both of these materials can be added to the asthenosphere to cause changes in the magma chamber. This further reveals the characteristics of high oxygen fugacity, rich in incompatible elements and the oxidation environment of magma in the BA source area. However, DA in the study area shows obvious geochemical characteristics of high-K volcanic rocks, which further indicates that the magma was produced far from the arc magma center, and the magma source area is relatively stable, which is not the product of intense extrusion collision mode (Raymond et al., 2020; Gong et al., 2021a). Combined with the DA relaxed magmatic-tectonic environment indication and the BA marginal extensional rift environment discrimination, the subduction model in the study area is similar to the low-angle slab subduction model established by predecessors. The new young oceanic crust in the Paleo-Pacific Ocean at this time also provided the prerequisite for low-angle subduction. The relative extension "detachment" tectonic environment is also conducive to the continuous eruption of magma over a large area. Many crust-derived materials are wrapped by Paleo-Pacific Ocean slab subduction. When slab subduction reached a certain depth and position, a large amount of melt (fluid) formed by continuous plate dehydration continued to weaken the lithospheric

mantle and form EM-II mantle characteristics, resulting in the unique complex geochemical properties of the BA in the study area. A large amount of lithospheric mantle and lower crust with the intensification of underplating began to partially melt to form the DA parent magma, and the gradual thinning of the crust formed a large number of tensile fractures. BA and DA magma chambers erupted along these fractures under pressure to form the Late Triassic volcanic rocks of the Meiji Reef.

Ishikawa and Tera (1997) studied a large number of underwater volcanoes in the Chiba arc and found that they may have formed in a rear-arc environment, which mainly produced a series of tholeiites, from calc-alkaline basalt to rhyolite, mainly basaltic andesite, which is clearly different from back-arc basalt. Peate et al. (1997) also pointed out that Vanuatu island-arc magma in the southwestern Pacific Ocean may be of the "rear-arc" type, which has a low degree of magma melting and is a K-containing volcanic rock series at the farthest end of the arc magma. The geochemical properties of the two series rocks in the study area are well consistent with the above characteristics, and the tectonic spatio-temporal properties also have rear-arc characteristics. Therefore, it is considered that the study area probably belongs to this obvious rear-arc tectonic environment, and the two series of rocks belong to the farthest part of the arc magma. Combined with the characteristics of geochronology, it is concluded that the western margin of the Paleo-Pacific Ocean began to subduct to the ancient land of South China during the Late Triassic, a mature arc magmatic system was formed, and back-arc extensional tectonics gradually formed. This extensional tectonics provided an incentive for the NB to split away from the ancient South China land, and the Late Triassic was very likely an important tectonic time point for detachment. It also indicates that the ancient South China land should have been a relatively relaxed passive continental margin at this time, and the western Pacific subduction mode should have been an Andean type (Pitcher et al., 1985).

The obvious extensional tectonic environment in the study area suggests that the SCC tectonics were not converted to the Paleo-Pacific tectonic domain at this time. Combined with the characteristics that the Changning-Menglian suture belt entered the postcontinental collision extension period and the Qinling-Dabieshan-Sulu collision belt entered the main collision period, it can be concluded that the southeastern margin of South China was still a passive collision during the Late Triassic period, which facilitated the subduction of the western Pacific Plate and resulted in the generation of a large number of back-arc rifts (Wu and Suppe, 2018). This has laid a foundation for the emergence of the detachment of a large number of islands in Southeast Asia (e.g., NB, Zhongsha Block, Mindoro Block, Palawan Block, etc.). During the Late Triassic, the NB was located near the back-arc extensional tectonics on one side of the continental margin (southeast margin of the SCC) under the subduction environment of the western Pacific Ocean and was subjected to obvious slab subduction of the Paleo-Pacific Ocean.

This "staged" slab subduction pattern of the Paleo-Pacific on the SCC indicates that the whole southeastern margin of the SCC was obviously influenced by the Paleo-Pacific tectonic domain during the Late Triassic, and the initiation of this large-scale tectonic domain had a profound impact on the whole SCC. For example, the large-scale mineralization in the SCC during the Late Triassic (high- and low-temperature W-Sn-Au-Sb-Pb-Zn metallogenic belt located east to west in the SCC during 230–200 Ma), oceanic and continental interaction sedimentary tectonics and Paleo-climatic abrupt change, and other important events occurred during this period. A large number of initial continental margin rifts formed by lithospheric crust thinning caused by Paleo-Pacific Plate slab subduction provide tectonic space for a large number of enriched deposits. This dynamic rhythmic open-close model facilitates the continuous differentiation of magma (conducive to the collection of metallogenic elements) and intrusion. This is the main reason why BA and DA are interbedded in the study area. We believe that the back-arc extensional environment caused by the subduction of the Paleo-Pacific Plate in the study area was an important cause to the separation of the NB from the ancient South China block. The Late Triassic, an important tectonic event node, is an important time point for the formation of the initial intracontinental rift in the SCS. The two series of volcanic rocks in Well NK-1 of the Meiji Reef provide strong support for this theory. However, the multistage tectonic movement after this time point led to the "intermittent" adjustment of the shape and boundary of the NB and finally created the current complex strike-slip and sag pattern (Fig.26).

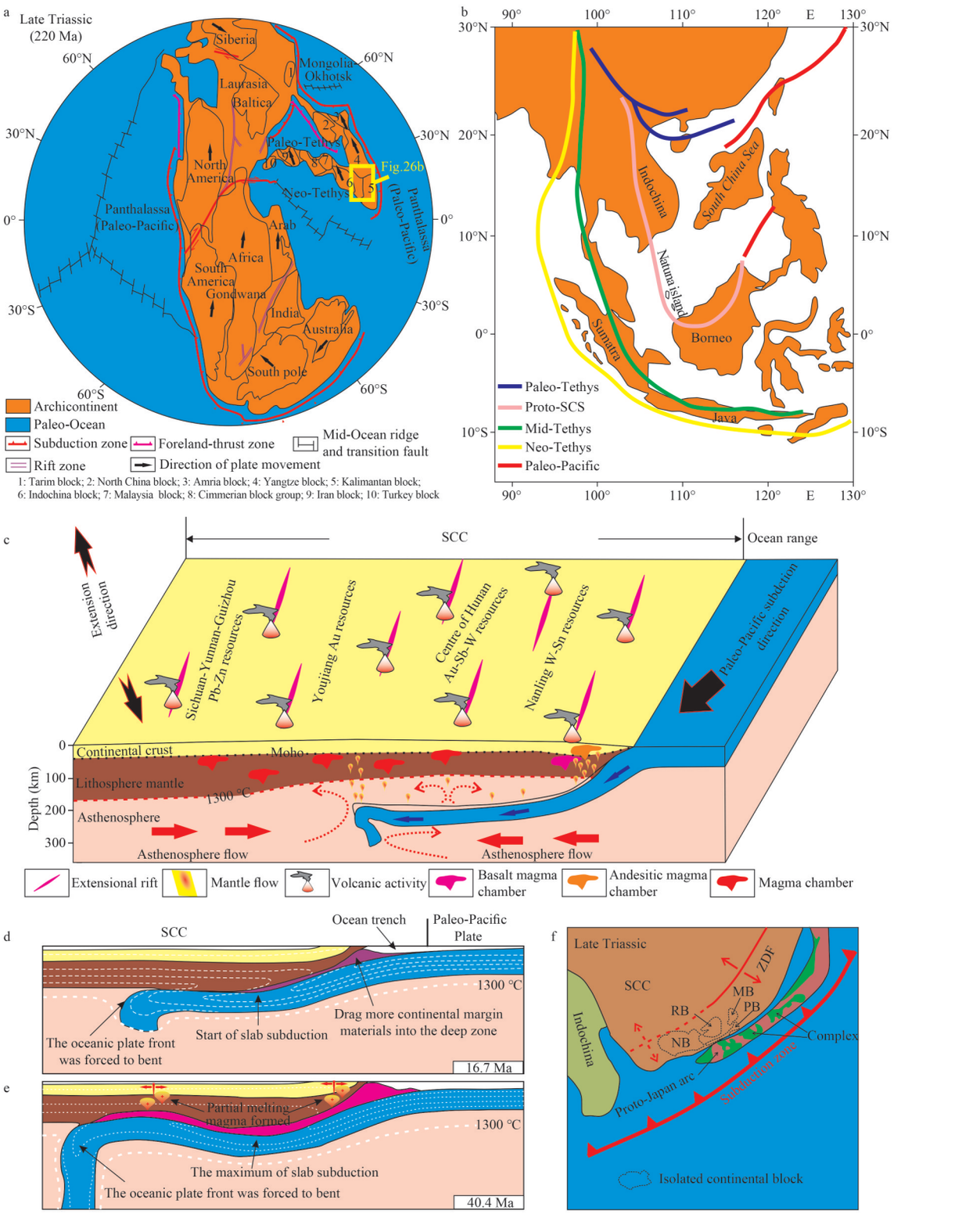

Fig.26 Global plate and tectonic scheme in the Late Triassic (after Taskyn et al. (2014)) (a); schematic of the spread of the Proto-SCS with the Tethys and the ancient Pacific (after Shi et al. (2020)) (b); Paleo-Pacific subduction magmatic-tectonic modelling (after Xie et al. (2021)) (c); computer simulation of diagram for the plate subduction process (after Li et al. (2018a)) (d & e); paleogeographic reconstructions of Southeast Asia in the Late Triassic (after Miao et al. (2021)) (f)

MB: Mindoro Block; NB: Nansha Block; PB: Palawan Block; RB: Reed Bank; ZDF: Zhenghe-Dapu Fault; SCC: South China Craton.

5 CONCLUSION

This detailed study on genetic mechanism of volcanic rocks in Well NK-1 of the Meiji Reef suggested the following:

(1) The volcanic rocks in Well NK-1 comprise 36 rhythmic layers encompassing an overflow phase and an intermittent eruption-overflow phase, and contain locally extreme cryptoexplosive breccia facies. These rocks can be further classified as a first mafic→neutral magmatic volcanic activity cycle (3 subcycles, in apparent thickness of 727.3 m) and a second mafic→intermediate-felsic magmatic volcanic activity cycle (including 3 subcycles, in apparent thickness of 294.0 m), which exhibits obvious characteristics of alkaline magma.

(2) Combining the geochronological and geochemical data of Well NK-1 published by our team, we can conclude that BA and DA were formed during the Late Triassic between 218.6±3.2 Ma and 217.9±3.5 Ma. The two series of rocks exhibit obvious island-arc magmatic properties and EM-II-typed magmatic characteristics. The PM-normalized spider diagram shows that BA exhibited more similar characteristics to those of LCC and was significantly enriched in incompatible elements. However, DA was more consistent with the UCC and enriched in crust-derived elements. The BA magma source area is partially melted, which is influenced by a large amount of subducted melt (fluid). The DA magma source area is dominated by fractional crystallization, and assimilation and contamination are very weak. The Sr-Nd-Pb-Hf isotopic characteristics of these two series rocks indicate obvious crust-mantle mixing. The BA source area reflects obvious influences of young oceanic crust and old crustal recycling, while the DA source area mainly indicates the addition of ancient crustal material.

(3) The geochemical characteristics of BA and DA are highly consistent with those of rear-arc magmas, showing enrichment characteristics of incompatible elements higher than those of MORB and lower than those of OIB, as well as enhanced isotopic properties. A large amount of sediment entrained by the Paleo-Pacific Ocean was slab subducted westward into the deep SCC, and continuous plate dehydration caused a large amount of melt (fluid) to join the asthenosphere on the side of the continent. Thus, the EM-II-typed source area was formed, where a large number of water-rich, volatile-rich fluids and recirculating sediment melts were continuously enriched.

Combining the Late Triassic tectonic geological background in the study area and the two series of tectonic attribute analysis data in this paper, it is proposed that the southeastern margin of the SCC at this time was still a passive continental margin, the magma eruption environment was a relatively extruded extensional environment, which was a phased "periodic open-close" tectonic system, and a mature island-arc system formed along the southeastern margin of the ancient South China continent during this period. The unique accordion-like periodic open-close movement may have reflected the main tectonic dynamic mechanism of the separation of the NB from the SCC, and thus, the back-arc extensional tectonics may have induced the formation of the initial continental rift in the SCS.

6 DATA AVAILABILITY STATEMENT

The data that support the findings of this study are available from Miao et al. (2021) (https://doi.org/10.1016/j.lithos.2021.106337) and Wei et al. (2022) (https://doi.org/10.1111/ter.12556).

7 ACKNOWLEDGMENT

We thank Xiuquan MIAO from Guangzhou Institute of Geochemistry, Chinese Academy of Sciences and Wu WEI from Institute of Geology and Geophysics, Chinese Academy of Sciences for their collaboration with our team and for their data contribution. We also thank Jianghong DENG and Bin DENG from Chengdu University of Technology for their help and advice in petrology and petrography. We are grateful to the Well NK-1 research team of the Key Laboratory of Ocean and Marginal Sea Geology, South China Sea Institute of Oceanology, for providing the core samples.

References

Altherr R, Holl A, Hegner E et al. 2000. High-potassium, calc-alkaline I-type plutonism in the European Variscides: northern Vosges (France) and northern Schwarzwald (Germany). *Lithos*, **50**(1-3): 51-73, https://doi.org/10.1016/S0024-4937(99)00052-3.

Arculus R J. 2004. Evolution of arc magmas and their volatiles. *In*: Sparks R S J, Hawkesworth C J eds. The State of the Planet: Frontiers and Challenges in Geophysics, Volume 150. American Geophysical Union, Washington. p.95-108, https://doi.org/10.1029/150GM09.

Batchelor R A, Bowden P. 1985. Petrogenetic interpretation of granitoid rock series using multicationic parameters. *Chemical Geology*, **48**(1-4): 43-55, https://doi.org/10.1016/0009-2541(85)90034-8.

Blichert-Toft J, Albarède F. 1999. Hf isotopic compositions of the Hawaii Scientific Drilling Project core and the source mineralogy of Hawaiian basalts. *Geophysical Research Letters*, **26**(7): 935-938, https://doi.org/10.1029/1999GL900110.

Caricchi L, Annen C, Blundy J et al. 2014. Frequency and magnitude of volcanic eruptions controlled by magma injection and buoyancy. *Nature Geoscience*, **7**(2): 126-130, https://doi.org/10.1038/ngeo2041.

Chen F, Cai F, Yang B H et al. 1992. Characterization of fine-grained turbidite deposits from the South China Sea sediment cores. *Chinese Journal of Oceanology and Limnology*, **10**(2): 184-192, https://doi.org/10.1007/BF02844750.

Chen H L, Zhu M, Chen S Q et al. 2020. Basin-orogen patterns and the late Triassic foreland basin conversion process in the western Yangtze Block, China. *Journal of Asian Earth Sciences*, **194**: 104311, https://doi.org/10.1016/j.jseaes.2020.104311.

Defant M J, Drummond M S. 1990. Derivation of some modern arc magmas by melting of young subducted lithosphere. *Nature*, **347**(6294): 662-665, https://doi.org/10.1038/347662a0.

Ding L, Yang D, Cai F L et al. 2013. Provenance analysis of the Mesozoic Hoh-Xil-Songpan-Ganzi turbidites in northern Tibet: implications for the tectonic evolution of the eastern Paleo-Tethys Ocean. *Tectonics*, **32**(1): 34-48, https://doi.org/10.1002/tect.20013.

Duan L, Meng Q R, Wu G L et al. 2020. Nanpanjiang Basin: a window on the tectonic development of South China during Triassic assembly of the southeastern and eastern Asia. *Gondwana Research*, **78**: 189-209, https://doi.org/10.1016/j.gr.2019.08.009.

Eby G N. 1992. Chemical subdivision of the A-type granitoids: petrogenetic and tectonic implications. *Geology*, **20**(7): 641-644, https://doi.org/10.1130/0091-7613(1992)020<0641:CSOTAT>2.3.CO;2.

Eby G N. 1990. The A-type granitoids: a review of their occurrence and chemical characteristics and speculations on their petrogenesis. *Lithos*, **26**(1-2): 115-134, https://doi.org/10.1016/0024-4937(90)90043-z.

Feio G R L, Dall'Agnol R, Dantas E L et al. 2012. Geochemistry, geochronology, and origin of the Neoarchean Planalto Granite suite, Carajás, Amazonian craton: a-type or hydrated charnockitic granites? *Lithos*, **151**: 57-73, https://doi.org/10.1016/j.lithos.2012.02.020.

Fitton J G, Saunders A D, Norry M J et al. 1997. Thermal and chemical structure of the Iceland plume. *Earth and Planetary Science Letters*, **153**(3-4): 197-208, https://doi.org/10.1016/S0012-821X(97)00170-2.

Gao P, Zheng Y F, Zhao Z F. 2017. Triassic granites in South China: a geochemical perspective on their characteristics, petrogenesis, and tectonic significance. *Earth-Science Reviews*, **173**: 266-294, https://doi.org/10.1016/j.earscirev.2017.07.016.

Gardien V, Thompson A B, Grujic D et al. 1995. Experimental melting of biotite+plagioclase+quartz± muscovite assemblages and implications for crustal melting. *Journal of Geophysical Research*: *Solid Earth*, **100**(B8): 15581-15591, https://doi.org/10.1029/95jb00916.

Gee D G, Klonowska I, Andréasson P G et al. 2020. Middle thrust sheets in the Caledonide orogen, Sweden: the outer margin of Baltica, the continent-ocean transition zone and late Cambrian-Ordovician subduction-accretion. *Geological Society*, *London*, *Memoirs*, **50**(1): 517-548, https://doi.org/10.1144/M50-2018-73.

Gong D X, Wu C H, Zou H et al. 2021a. Provenance analysis of Late Triassic turbidites in the eastern Songpan-Ganzi flysch complex: sedimentary record of tectonic evolution of the eastern Paleo-Tethys Ocean. *Marine and Petroleum Geology*, **126**: 104927, https://doi.org/10.1016/j.marpetgeo.2021.104927.

Gong D X, Xiao B, Bagas L et al. 2021b. Origin of the Early to Middle Triassic polyhalite minerals in the Sichuan Basin, SW China: new evidence from calcium and sulphur isotopes and microfabrics. *Ore Geology Reviews*, **139**: 104439, https://doi.org/10.1016/j.oregeorev.2021.104439.

Hall R. 2012. Late Jurassic-Cenozoic reconstructions of the Indonesian region and the Indian Ocean. *Tectonophysics*, **570-571**: 1-41, https://doi.org/10.1016/j.tecto.2012.04.021.

Hara H, Hirano M, Kurihara T et al. 2018. Permian arc evolution associated with Panthalassa subduction along the eastern margin of the South China block, based on sandstone provenance and U-Pb detrital zircon ages of the Kurosegawa belt, Southwest Japan. *Journal of Asian Earth Sciences*, **151**: 112-130, https://doi.org/10.1016/j.jseaes.2017.10.025.

Hernández-Uribe D, Palin R M, Cone K A et al. 2020. Petrological implications of seafloor hydrothermal alteration of subducted mid-ocean ridge basalt. *Journal of Petrology*, **61**(9): egaa086, https://doi.org/10.1093/petrology/egaa086.

Holloway N H. 1981. The North Palawan block, Philippines: its relation to the Asian mainland and its role in the evolution of the South China Sea. *Bulletin of the Geological Society of Malaysia*, **14**: 19-58, https://doi.org/10.7186/bgsm14198102.

Hong H L, Fang Q, Zhao L L et al. 2017. Weathering and alteration of volcanic ashes in various depositional settings during the Permian-Triassic transition in South China: mineralogical, elemental and isotopic approaches. *Palaeogeography*, *Palaeoclimatology*, *Palaeoecology*, **486**: 46-57, https://doi.org/10.1016/j.palaeo.2016.12.033.

Hora J M, Singer B S, Wörner G et al. 2009. Shallow and deep crustal control on differentiation of calc-alkaline and tholeiitic magma. *Earth and Planetary Science Letters*, **285**(1-2): 75-86, https://doi.org/10.1016/j.epsl.2009.05.042.

Hoskin P W O, Schaltegger U. 2003. The composition of zircon and igneous and metamorphic petrogenesis. *Reviews in Mineralogy and Geochemistry*, **53**(1): 27-62, https://doi.org/10.2113/0530027.

Hou L, Xiong F H, Wang W et al. 2019. Carboniferous-Triassic felsic igneous rocks and typical mineral deposits in the Truong Son orogenic belt, SE Asia: implications for Paleo-Tethyan tectonic evolution and metallogeny. *Ore Geology Reviews*, **112**: 103036, https://doi.org/10.1016/j.oregeorev.2019.103036.

Huang X L, Niu Y L, Xu Y G et al. 2013. Geochronology and geochemistry of Cenozoic basalts from eastern Guangdong, SE China: constraints on the lithosphere evolution beneath the northern margin of the South China Sea. *Contributions to Mineralogy and Petrology*, **165**(3): 437-455, https://doi.org/10.1007/s00410-012-0816-7.

Ishikawa T, Tera F. 1997. Source, composition and distribution of the fluid in the Kurile mantle wedge: constraints from across-arc variations of B/Nb and B isotopes. *Earth and Planetary Science Letters*, **152**(1-4): 123-138, https://doi.org/10.1016/S0012-821X(97)00144-1.

Iwamori H, Nakamura H. 2015. Isotopic heterogeneity of oceanic, arc and continental basalts and its implications for mantle dynamics. *Gondwana Research*, **27**(3): 1131-1152, https://doi.org/10.1016/j.gr.2014.09.003.

Jahn B M. 2010. Accretionary orogen and evolution of the Japanese Islands: implications from a Sr-Nd isotopic study of the Phanerozoic granitoids from SW Japan. *American Journal of Science*, **310**(10): 1210-1249, https://doi.org/10.2475/10.2010.02.

Jian X, Weislogel A, Pullen A. 2019. Triassic sedimentary filling and closure of the eastern Paleo-Tethys Ocean: new insights from detrital zircon geochronology of Songpan-Ganzi, Yidun, and West Qinling flysch in eastern Tibet. *Tectonics*, **38**(2): 767-787, https://doi.org/10.1029/2018TC005300.

Kelley K A, Plank T, Newman S et al. 2010. Mantle melting as a function of water content beneath the Mariana Arc. *Journal of Petrology*, **51**(8): 1711-1738, https://doi.org/10.1093/petrology/egq036.

Kong H L, Dong G C, Mo X X et al. 2012. Petrogenesis of Lincang granites in Sanjiang area of western Yunnan Province: constraints from geochemistry, zircon U-Pb geochronology and Hf isotope. *Acta Petrologica Sinica*, **28**(5): 1438-1452, https://doi.org/CNKI:SUN:YSXB.0.2012-05-010. (in Chinese with English abstract)

Labanieh S, Chauvel C, Germa A et al. 2012. Martinique: a clear case for sediment melting and slab dehydration as a function of distance to the trench. *Journal of Petrology*, **53**(12): 2441-2464, https://doi.org/10.1093/petrology/egs055.

Le Bas M J, Le Maitre R W, Streckeisen A et al. 1986. A chemical classification of volcanic rocks based on the total Alkali-Silica diagram. *Journal of Petrology*, **27**(3): 745-750, https://doi.org/10.1093/petrology/27.3.745.

Le Breton N, Thompson A B. 1988. Fluid-absent (dehydration) melting of biotite in metapelites in the early stages of crustal anatexis. *Contributions to Mineralogy and Petrology*, **99**(2): 226-237, https://doi.org/10.1007/BF00371463.

Li S G. 1993. Ba-Nb-Th-La diagrams used to identify tectonic environments of ophiolite. *Acta Petrologica Sinica*, **9**(2): 146-157. (in Chinese with English abstract)

Li S M, Wang Q, Zhu D C et al. 2022. Formation of continental crust by diapiric melting of recycled crustal materials in the mantle wedge. *Geophysical Research Letters*, **49**(15): e2021GL097515, https://doi.org/10.1029/2021GL097515.

Li S Z, Suo Y H, Li X Y et al. 2018a. Mesozoic plate subduction in West Pacific and tectono-magmatic response in the East Asian ocean-continent connection zone. *Chinese Science Bulletin*, **63**(16): 1550-1593, https://doi.org/10.1360/N972017-01113. (in Chinese with English abstract)

Li S Z, Zang Y B, Wang P C et al. 2017. Mesozoic tectonic transition in South China and initiation of Palaeo-Pacific subduction. *Earth Science Frontiers*, **24**(4): 213-225, https://doi.org/10.13745/j.esf.yx.2017-4-13. (in Chinese with English abstract)

Li X C, Zhou M F. 2018. The nature and origin of hydrothermal REE Mineralization in the Sin Quyen deposit, Northwestern Vietnam. *Economic Geology*, **113**(3): 645-673, https://doi.org/10.5382/econgeo.2018.4565.

Li X C, Zhou M F, Chen W T et al. 2018b. Uranium-lead dating of hydrothermal zircon and monazite from the Sin Quyen Fe-Cu-REE-Au- (U) deposit, northwestern Vietnam. *Mineralium Deposita*, **53**(3): 399-416, https://doi.org/10.1007/s00126-017-0746-4.

Li X H, Li Z X, He B et al. 2012. The Early Permian active continental margin and crustal growth of the Cathaysia Block: *in situ* U-Pb, Lu-Hf and O isotope analyses of detrital zircons. *Chemical Geology*, **328**: 195-207, https://doi.org/10.1016/j.chemgeo.2011.10.027.

Li X H, Li W X, Li Z X et al. 2009. Amalgamation between the Yangtze and Cathaysia Blocks in South China: constraints from SHRIMP U-Pb zircon ages, geochemistry and Nd-Hf isotopes of the Shuangxiwu volcanic rocks. *Precambrian Research*, **174**(1-2): 117-128, https://doi.org/10.1016/j.precamres.2009.07.004.

Liu H, Wang C, Deng B et al. 2019a. Geochemical characteristics and thermal evolution of Paleogene source rocks in Lunpola Basin, Tibet Plateau. *Petroleum Science and Technology*, **37**(8): 950-961, https://doi.org/10.1080/10916466.2019.1575870.

Liu H, Wang C, Deng J H et al. 2021a. Evaluation of sedimentary features and biomarkers in the Paleogene Niubao formation in the Lunpola basin, Tibetan Plateau: implications for the oil source rocks and exploration. *International Journal of Earth Sciences*, **110**(2): 399-417, https://doi.org/10.1007/s00531-020-01958-x.

Liu H, Wang C, Li Y et al. 2021b. Geochemistry of the black rock series of lower Cambrian Qiongzhusi Formation, SW Yangtze Block, China: reconstruction of sedimentary and tectonic environments. *Open Geosciences*, **13**(1): 166-187, https://doi.org/10.1515/geo-2020-0228.

Liu J G, Cao L, Yan W et al. 2019b. New archive of another significant potential sediment source in the South China Sea. *Marine Geology*, **410**: 16-21, https://doi.org/10.1016/j.margeo.2019.01.003.

Liu Y, Xiao W J, Windley B F et al. 2019c. Late Triassic ridge subduction of Paleotethys: insights from high-Mg granitoids in the Songpan-Ganzi area of northern Tibet. *Lithos*, **334-335**: 254-272, https://doi.org/10.1016/j.lithos.2019.03.012.

Liu Z S, Yan P, Liu H L. 1997. On the origin age of the Southwest Basin in the South China Sea. *Chinese Journal of Oceanology and Limnology*, **15**(3): 285-288,

https://doi.org/10.1007/BF02850886.

Luo Y, Li G, Xu W H et al. 2021. The effect of diagenesis on rare earth element geochemistry of the Quaternary carbonates at an isolated coral atoll in the South China Sea. *Sedimentary Geology*, **420**: 105933, https://doi.org/10.1016/j.sedgeo.2021.105933.

Maniar P D, Piccoli P M. 1989. Tectonic discrimination of granitoids. *Geological Society of America Bulletin*, **101**(5): 635-643, https://doi.org/10.1130/0016-7606(1989)101<0635:TDOG>2.3.CO;2.

Meschede M. 1986. A method of discriminating between different types of mid-ocean ridge basalts and continental tholeiites with the Nb-Zr-Y diagram. *Chemical Geology*, **56**(3-4): 207-218, https://doi.org/10.1016/0009-2541(86)90004-5.

Miao X Q, Huang X L, Yan W et al. 2021. Late Triassic dacites from Well NK-1 in the Nansha Block: constraints on the Mesozoic tectonic evolution of the southern South China Sea margin. *Lithos*, **398-399**: 106337, https://doi.org/10.1016/j.lithos.2021.106337.

Milani L, Lehmann J, Naydenov K V et al. 2015. A-type magmatism in a syn-collisional setting: the case of the Pan-African Hook Batholith in Central Zambia. *Lithos*, **216-217**: 48-72, https://doi.org/10.1016/j.lithos.2014.11.029.

Miller C, Schuster R, Klötzli U et al. 1999. Post-collisional potassic and ultrapotassic magmatism in SW Tibet: geochemical and Sr-Nd-Pb-O isotopic constraints for mantle source characteristics and petrogenesis. *Journal of Petrology*, **40**(9): 1399-1424, https://doi.org/10.1093/petroj/40.9.1399.

Müller D, Groves D I. 2000. Potassic Igneous Rocks and Associated Gold-Copper Mineralization. Springer, Berlin, Heidelberg. 297p, https://doi.org/10.2113/econgeo.111.3.796.

Nicolae I, Saccani E. 2003. Petrology and geochemistry of the Late Jurassic calc-alkaline series associated to Middle Jurassic ophiolites in the South Apuseni Mountains (Romania). *Swiss Journal of Geosciences Supplement*, **83**(1): 81-96, https://doi.org/10.1146/annurev.ento.42.1.393.

Patiño Douce A E. 1996. Effects of pressure and H_2O content on the compositions of primary crustal melts. *Earth and Environmental Science Transactions of the Royal Society of Edinburgh*, **87**(1-2): 11-21, https://doi.org/10.1017/S026359330000643X..

Patiño Douce A E. 1997. Generation of metaluminous A-type granites by low-pressure melting of calc-alkaline granitoids. *Geology*, **25**(8): 743-746, https://doi.org/10.1130/0091-7613(1997)025<0743:GOMATG>2.3.CO;2.

Patiño Douce A E, Beard J S. 1995. Dehydration-melting of biotite gneiss and quartz amphibolite from 3 to 15 kbar. *Journal of Petrology*, **36**(3): 707-738, https://doi.org/10.1093/petrology/36.3.707.

Patiño Douce A E, Johnston A D. 1991. Phase equilibria and melt productivity in the politic system: implications for the origin of peraluminous granitoids and aluminous granulites. *Contributions to Mineralogy and Petrology*, **107**(2): 202-218, https://doi.org/10.1007/BF00310707.

Pearce J A. 1982. Trace element characteristics of lavas from destructive plate boundaries. *In*: Thorps R S ed. Andesites. John Wiley and Sons, New York. p.525-548.

Pearce J A. 2008. Geochemical fingerprinting of oceanic basalts with applications to ophiolite classification and the search for Archean oceanic crust. *Lithos*, **100**(1-4): 14-48, https://doi.org/10.1016/j.lithos.2007.06.016.

Pearce J A, Cann J R. 1973. Tectonic setting of basic volcanic rocks determined using trace element analyses. *Earth and Planetary Science Letters*, **19**(2): 290-300, https://doi.org/10.1016/0012-821X(73)90129-5.

Pearce J A, Harris N B W, Tindle A G. 1984. Trace element discrimination diagrams for the tectonic interpretation of granitic rocks. *Journal of Petrology*, **25**(4): 956-983, https://doi.org/10.1093/petrology/25.4.956.

Pearce J A, Norry M J. 1979. Petrogenetic implications of Ti, Zr, Y, and Nb variations in volcanic rocks. *Contributions to Mineralogy and Petrology*, **69**(1): 33-47, https://doi.org/10.1007/BF00375192.

Pearce J A, Stern R J, Bloomer S H et al. 2005. Geochemical mapping of the Mariana arc-basin system: implications for the nature and distribution of subduction components. *Geochemistry*, *Geophysics*, *Geosystems*, **6**(7): Q07006, https://doi.org/10.1029/2004GC000895.

Peate D W, Pearce J A, Hawkesworth C et al. 1997. Geochemical variations in Vanuatu Arc Lavas: the role of subducted material and a variable mantle wedge composition. *Journal of Petrology*, **38**(10): 1331-1358, https://doi.org/10.1093/petrology/38.10.1331.

Pitcher W S, Atherton M P, Cobbing E J et al. 1985. Magmatism at a Plate Edge: The Peruvian Andes. Blackie Halstead Press, Glasgow. 328p.

Rapp R P, Watson E B. 1995. Dehydration melting of metabasalt at 8-32 kbar: implications for continental growth and crust-mantle recycling. *Journal of Petrology*, **36**(4): 891-931, https://doi.org/10.1093/petrology/36.4.891.

Raymond L A, Ogawa Y, Maddock M E. 2020. Accretionary unit formats in subduction complexes: examples from the Franciscan and Miura-Boso complexes. *International Geology Review*, **62**(12): 1581-1609, https://doi.org/10.1080/00206814.2019.1667881.

Shao W Y, Chung S L, Chen W S et al. 2015. Old continental zircons from a young oceanic arc, eastern Taiwan: implications for Luzon subduction initiation and Asian accretionary orogeny. *Geology*, **43**(6): 479-482, https://doi.org/10.1130/G36499.1.

Shervais J W. 1982. Ti-V plots and the petrogenesis of modern and ophiolitic lavas. *Earth and Planetary Science Letters*, **59**(1): 101-118, https://doi.org/10.1016/0012-821X(82)90120-0.

Shi H Y, Li T L, Zhang R Z et al. 2020. Imaging of the upper mantle beneath Southeast Asia: constrained by teleseismic P-wave tomography. *Remote Sensing*, **12**(18): 2975, https://doi.org/10.3390/rs12182975.

Shu L S, Zhu W B, Xu Z Q. 2021. Geological settings and metallogenic conditions of the granite-type lithium ore deposits in South China. *Acta Geologica Sinica*, **95**(10): 3099-3114, https://doi.org/10.19762/j.cnki.dizhixuebao.2021152. (in Chinese with English abstract)

Singh J, Johannes W. 1996. Dehydration melting of tonalites.

Part II. Composition of melts and solids. *Contributions to Mineralogy and Petrology*, **125**(1): 26-44, https://doi.org/10.1007/s004100050204.

Skjerlie K P, Johnston A D. 1993. Fluid-absent melting behavior of an F-rich tonalitic gneiss at mid-crustal pressures: implications for the generation of anorogenic granites. *Journal of Petrology*, **34**(4): 785-815, https://doi.org/10.1093/petrology/34.4.785.

Stevenson D S. 2018. Granite Skyscrapers: How Rock Shaped Earth and Other Worlds. Praxis Publishing, Chichester, UK. 374p, https://doi.org/10.1007/978-3-319-91503-6.

Sun K, Wu T, Liu X S et al. 2020. Lithogeochemistry of the mid-ocean ridge basalts near the Fossil Ridge of the Southwest Sub-Basin, South China Sea. *Minerals*, **10**(5): 465, https://doi.org/10.3390/min10050465.

Sun S Q, Wang Y L, Zhang C J. 2003. Discrimination of the tectonic settings of basalts by Th, Nb and Zr. *Geological Review*, **49**(1): 40-47, https://doi.org/10.16509/j.georeview.2003.01.006. (in Chinese with English abstract)

Sun S S, McDonough W F. 1989. Chemical and isotopic systematics of oceanic basalts: implications for mantle composition and processes. *Geological Society of London*, Special Publications, **42**(1): 313-345, https://doi.org/10.1144/GSL.SP.1989.042.01.19.

Sun Y, Wu T, Xiao L et al. 2019. U-Pb ages, Hf-O isotopes and trace elements of zircons from the ore-bearing and ore-barren adakitic rocks in the Handan-Xingtai district: implications for petrogenesis and iron mineralization. *Ore Geology Reviews*, **104**: 14-25, https://doi.org/10.1016/j.oregeorev.2018.10.010.

Sylvester P J. 1998. Post-collisional strongly peraluminous granites. *Lithos*, **45**(1-4): 29-44, https://doi.org/10.1016/S0024-4937(98)00024-3.

Taskyn A, Li J H, Li W B et al. 2014. Research on global paleo-plate reconstuction and lithofacies palaeogeography in Triassic. *Marine Geology & Quaternary Geology*, **34**(5): 153-162, https://doi.org/10.3724/SP.J.1140.2014.05153. (in Chinese with English abstract)

Taylor S R, McLennan S M. 1985. The Continental Crust: Its Composition and Evolution. ScientificBlackwell, Oxford, London, Edinburgh, Boston, AltoPalo, Melbourne. 312p.

Tollan P, Hermann J. 2019. Arc magmas oxidized by water dissociation and hydrogen incorporation in orthopyroxene. *Nature Geoscience*, **12**(8): 667-671, https://doi.org/10.1038/s41561-019-0411-x.

Turner S P, George R M M, Evans P J et al. 2000. Time-scales of magma formation, ascent and storage beneath subduction-zone volcanoes. *Philosophical Transactions of the Royal Society A*: *Mathematical*, *Physical and Engineering Sciences*, **358**(1770): 1443-1464, https://doi.org/10.1098/rsta.2000.0598.

Valentine G A, Graettinger A H, Sonder I. 2014. Explosion depths for phreatomagmatic eruptions. *Geophysical Research Letters*, **41**(9): 3045-3051, https://doi.org/10.1007/s00445-017-1177-x.

Wang C, Liu H, Deng J H et al. 2018. Isotope geochronologic and geochemical constraints on the magmatic associations of the collisional orogenic zone in the west Kunlun Orogen, China. *Acta Geologica Sinica* (*English Edition*), **92**(2): 482-498, https://doi.org/10.1111/1755-6724.13538.

Wang C, Liu H, Feng H B et al. 2019. Geochemistry and U-Pb ages of the diabases from the Luoji area, western Yunnan, China: implications for the timing of the initial rifting of the Ganzi-Litang Ocean. *Geologia Croatica*, **72**: 19-32, https://doi.org/10.4154/gc.2019.25.

Wang J, Li Z X. 2001. Sequence stratigraphy and evolution of the Neoproterozoic marginal basins along southeastern Yangtze Craton, South China. *Gondwana Research*, **4**(1): 17-26, https://doi.org/10.1016/S1342-937X(05)70651-1.

Wang J, Li Z X. 2003. History of Neoproterozoic rift basins in South China: implications for Rodinia break-up. *Precambrian Research*, **122**(1-4): 141-158, https://doi.org/10.1016/S0301-9268(02)00209-7.

Wang K, Plank T, Walker J D et al. 2002. A mantle melting profile across the Basin and Range, SW USA. *Journal of Geophysical Research*: *Solid Earth*, **107**(B1): ECV 5-1-ECV 5-21, https://doi.org/10.1029/2001jb000209.

Wang W L, Dong D D, Wang X J et al. 2021. Three-stage tectonic subsidence and its implications for the evolution of conjugate margins of the southwest subbasin, South China Sea. *Journal of Oceanology and Limnology*, **39**(5): 1854-1870, https://doi.org/10.1007/s00343-020-0259-3.

Wei W, Liu C Z, Hou Y F et al. 2022. Discovery of a hidden Triassic arc in the Southern South China Sea: evidence for the breakaway of a ribbon continent with implications for the evolution of the Western Pacific margin. *Terra Nova*, **34**(1): 12-19, https://doi.org/10.1111/ter.12556.

Whalen J B, Currie K L, Chappell B W. 1987. A-type granites: geochemical characteristics, discrimination and petrogenesis. *Contributions to Mineralogy and Petrology*, **95**(4): 407-419, https://doi.org/10.1007/BF00402202.

Winchester J A, Floyd P A. 1977. Geochemical discrimination of different magma series and their differentiation products using immobile elements. *Chemical Geology*, **20**: 325-343, https://doi.org/10.1016/0009-2541(77)90057-2.

Wood D A. 1980. The application of a Th-Hf-Ta diagram to problems of tectonomagmatic classification and to establishing the nature of crustal contamination of basaltic lavas of the British Tertiary Volcanic Province. *Earth and Planetary Science Letters*, **50**(1): 11-30, https://doi.org/10.1016/0012-821x(80)90116-8.

Wu J, Suppe J. 2018. Proto-South China Sea Plate tectonics using subducted slab constraints from tomography. *Journal of Earth Science*, **29**(6): 1304-1318, https://doi.org/10.1007/s12583-017-0813-x.

Wu L N, Wang Z C, Wang Y L. 2003. On the application of La, Nb and Zr in identifying the tectonic settings. *Journal of East China Geological Institute*, **26**(4): 343-348, https://doi.org/CNKI:SUN:HDDZ.0.2003-04-006. (in Chinese with English abstract)

Wu T, Wang X C, Li W X et al. 2019. Petrogenesis of the ca. 820-810 Ma felsic volcanic rocks in the Bikou Group: implications for the tectonic setting of the western

margin of the Yangtze Block. *Precambrian Research*, **331**: 105370, https://doi.org/10.1016/j.precamres.2019.105370.

Xie G Q, Mao J W, Zhang C Q et al. 2021. Triassic deposits in South China: geological characteristics, ore-forming mechanism and ore deposit model. *Earth Science Frontiers*, **28**(3): 252-270, https://doi.org/10.13745/j.esf.sf.2021.1.26. (in Chinese with English abstract)

Xu C H, Zhang L, Shi H S et al. 2017. Tracing an early Jurassic magmatic arc from South to East China Seas. *Tectonics*, **36**(3): 466-492, https://doi.org/10.1002/2016TC004446.

Xu W C, Luo B J, Xu Y J et al. 2018. Geochronology, geochemistry, and petrogenesis of late Permian to early Triassic mafic rocks from Darongshan, South China: implications for ultrahigh-temperature metamorphism and S-type granite generation. *Lithos*, **308-309**: 168-180, https://doi.org/10.1016/j.lithos.2018.03.004.

Xu W H, Lin T, Hu Z H et al. 2012. Environmental exposure and ecological risk of heavy metals in fishing harbors of the Pearl River Delta, South China. *Aquatic Ecosystem Health & Management*, **15**(2): 192-199, https://doi.org/10.1080/14634988.2012.688484.

Yan Q S, Metcalfe I, Shi X F. 2017. U-Pb isotope geochronology and geochemistry of granites from Hainan Island (northern South China Sea margin): constraints on late Paleozoic-Mesozoic tectonic evolution. *Gondwana Research*, **49**: 333-349, https://doi.org/10.1016/j.gr.2017.06.007.

Yan Q S, Shi X F, Li N S. 2011. Oxygen and lead isotope characteristics of granitic rocks from the Nansha block (South China Sea): implications for their petrogenesis and tectonic affinity. *Island Arc*, **20**(2): 150-159, https://doi.org/10.1111/j.1440-1738.2010.00754.x.

Yan Z Y, Chen L, Xiong X et al. 2020. Observations and modeling of flat subduction and its geological effects. *Science China Earth Sciences*, **63**(8): 1069-1091, https://doi.org/10.1007/s11430-019-9575-2.

Yang J H, Zhang J H, Chen J Y et al. 2021. Mesozoic continental crustal rejuvenation of South China: insights from zircon Hf-O isotopes of early Jurassic gabbros, syenites and A-type granites. *Lithos*, **402-403**: 105678, https://doi.org/10.1016/j.lithos.2020.105678.

Yang W R, Zheng J D. 2002. Panorama on theory opening-closing tectonics of China. *Geological Science and Technology Information*, **21**(4): 31-34, https://doi.org/10.3969/j.issn.1000-7849.2002.04.007. (in Chinese with English abstract)

Yi L, Deng C L, Yan W et al. 2021. Neogene-Quaternary magnetostratigraphy of the biogenic reef sequence of core NK-1 in Nansha Qundao, South China Sea. *Science Bulletin*, **66**(3): 200-203, https://doi.org/10.1016/j.scib.2020.08.014.

Yu Y, Huang X L, Sun M et al. 2020. Missing Sr-Nd isotopic decoupling in subduction zone: decoding the multi-stage dehydration and melting of subducted slab in the Chinese Altai. *Lithos*, **362-363**: 105465, https://doi.org/10.1016/j.lithos.2020.105465.

Zartman R E, Haines S M. 1988. The plumbotectonic model for Pb isotopic systematics among major terrestrial reservoirs-a case for bidirectional transport. *Geochimica et Cosmochimica Acta*, **52**(6): 1327-1339, https://doi.org/10.1016/0016-7037(88)90204-9.

Zhang G J, Zhang X L, Zhou C Y et al. 2021. A new high-resolution $\delta^{13}C_{carb}$ record for the Early-Middle Triassic: insights from the Tianshengqiao section, South China. *Journal of University of Science and Technology of China*, **51**(6): 459-467, https://doi.org/10.52396/JUST-2021-0128.

Zhang Q, Jin W J, Li C D et al. 2010. Revisiting the new classification of granitic rocks based on whole-rock Sr and Yb contents. *Acta Petrologica Sinica*, **26**(4): 985-1015, https://doi.org/CNKI:SUN:YSXB.0.2010-12-002.

Zhang X J, Takeuchi M, Ohkawa M et al. 2018. Provenance of a Permian accretionary complex (Nishiki Group) of the Akiyoshi Belt in southwest Japan and paleogeographic implications. *Journal of Asian Earth Sciences*, **167**: 130-138, https://doi.org/10.1016/j.jseaes.2018.01.005.

Zhao D P, Maruyama S, Omori S. 2007. Mantle dynamics of Western Pacific and East Asia: insight from seismic tomography and mineral physics. *Gondwana Research*, **11**(1-2): 120-131, https://doi.org/10.1016/j.gr.2006.06.006.

Zhao L, Guo F, Fan W M et al. 2016. Early Cretaceous potassic volcanic rocks in the Jiangnan Orogenic Belt, East China: crustal melting in response to subduction of the Pacific-Izanagi ridge? *Chemical Geology*, **437**: 30-43, https://doi.org/10.1016/j.chemgeo.2016.05.011.

Zhu H L, Du L, Zhang Z F et al. 2020. Calcium isotopic signatures of depleted mid-ocean ridge basalts from the northeastern Pacific. *Journal of Oceanology and Limnology*, **38**(5): 1476-1487, https://doi.org/10.1007/s00343-020-0045-2.

Zimmer M M, Plank T, Hauri E H et al. 2010. The role of water in generating the calc-alkaline trend: new volatile data for Aleutian magmas and a new tholeiitic index. *Journal of Petrology*, **51**(12): 2411-2444, https://doi.org/10.1093/petrology/egq062.

Zindler A, Hart S. 1986. Chemical geodynamics. *Annual Review of Earth and Planetary Sciences*, **14**: 493-571, https://doi.org/10.1146/annurev.ea.14.050186.002425.

Zou H, Bagas L, Li X Y et al. 2020. Origin and evolution of the neoproterozoic dengganping granitic complex in the western margin of the Yangtze Block, SW China: implications for breakup of Rodina Supercontinent. *Lithos*, **370-371**: 105602, https://doi.org/10.1016/j.lithos.2020.105602.

Zou H, Li Q L, Bagas L et al. 2021. A Neoproterozoic low-$\delta^{18}O$ magmatic ring around South China: implications for configuration and breakup of Rodinia supercontinent. *Earth and Planetary Science Letters*, **575**: 117196, https://doi.org/10.1016/j.epsl.2021.117196.

Electronic supplementary material

Supplementary material (Supplementary Tables S1–S5) is available in the online version of this article at https://doi.org/10.1007/s00343-023-2347-7.